Remote Sensing of Environment 295 (2023) 113696

Contents lists available at ScienceDirect

Remote Sensing of Environment

journal homepage: www.elsevier.com/locate/rse

BESSv2.0: A satellite-based and coupled-process model for quantifying long-term global land–atmosphere fluxes

Bolun Li [a], Youngryel Ryu [a,b,*], Chongya Jiang [c], Benjamin Dechant [a,d,e], Jiangong Liu [a], Yulin Yan [f], Xing Li [a]

[a] Research Institute of Agriculture and Life Sciences, Seoul National University, Seoul, South Korea
[b] Department of Landscape Architecture and Rural Systems Engineering, Seoul National University, Seoul, South Korea
[c] College of Agricultural, Consumer and Environmental Sciences, University of Illinois at Urbana Champaign, Urbana, IL, USA
[d] German Centre for Integrative Biodiversity Research (iDiv), Halle-Jena-Leipzig, Leipzig, Germany
[e] Leipzig University, Leipzig, Germany
[f] Interdisciplinary Program in Agricultural and Forest Meteorology, Seoul National University, South Korea

ARTICLE INFO

Edited by Jing M. Chen

ABSTRACT

Recent remote-sensing-based global carbon, water and energy budgets over land still include considerable uncertainties. Most existing flux products of terrestrial carbon, water and energy components were developed individually, despite the inherently coupled processes among them. In this study, we present a new set of global daily surface downwelling shortwave radiation (SW), net radiation (R_{net}), evapotranspiration (ET), gross primary productivity (GPP), terrestrial ecosystem respiration (TER) and net ecosystem exchange (NEE) datasets at 0.05° resolutions from 1982 to 2019, by improving a satellite-based and coupled-process model—the Breathing Earth System Simulator (BESS). The new version of BESS (v2.0) integrated a newly developed ecosystem respiration module, an optimality-based maximum carboxylation rate (V_{cmax}) model, and extended the temporal coverage of flux datasets from 1982 to 2019. We evaluated BESS products against the FLUXNET2015 dataset at the site scale, and against several remote sensing and/or machine learning products on a global scale. At the site scale, BESS products agreed well with FLUXNET measurements, capturing 84%, 53%, 65%, 51% and 31% of daily variation in R_{net}, ET, GPP, TER and NEE, respectively. Interannual variation in BESS NEE showed relatively low consistency with the FLUXNET measurements, while the rest fluxes explained approximately half of the interannual variation. On a global scale, we found marked discrepancies in spatio-temporal patterns between BESS and several benchmark products. Over the period 1982–2019, BESSv2.0 estimated the mean annual global R_{net}, ET, GPP, TER and NEE to be 340.97 ± 5.22 ZJ yr^{-1} (mean ± 1 SD), 67.67 ± 0.71 10^3 km^3 yr^{-1}, 125.74 ± 5.95 Pg C yr^{-1}, 109.30 ± 3.16 Pg C yr^{-1}, and − 16.28 ± 2.95 Pg C yr^{-1}, respectively, with significant annual linear trends ($P < 0.01$) by −0.05 10^3 km^3 yr^{-2} for ET, by 0.52 Pg C yr^{-2} for GPP, by 0.28 Pg C yr^{-2} for TER, and by −0.25 Pg C yr^{-2} for NEE. We further evaluated various coupled processes derived by BESS in terms of functional properties (i.e., Budyko relation, carbon-use efficiency, water-use efficiency, and light-use efficiency), which agreed well with FLUXNET observations, unlike the benchmark products. Overall, BESSv2.0 can serve as a set of reliable and independent products from other global satellite products, facilitating studies related to global carbon, water and energy budgets in a coupled and comprehensive manner.

1. Introduction

Improving our knowledge of the exchange of carbon, water, and energy fluxes in and out of terrestrial ecosystems is crucial for monitoring the state of the Earth's climate system (Chapin et al., 2006; Piao et al., 2020; Ryu et al., 2011). Accumulated observational evidence implies that these terrestrial ecosystem cycles are inherently tightly coupled, and are modulated by a suite of ecosystem functional properties such as the Budyko relation and carbon-(CUE), water-(WUE) and light-(LUE) use efficiency (Baldocchi and Meyers, 1998; Leuning et al., 1995a; Ryu et al., 2011). For example, the Budyko relation (Budyko, 1974; Sposito, 2017) quantifies annual evapotranspiration (ET) based

* Corresponding author at: Department of Landscape Architecture and Rural Systems Engineering, Seoul National University, Seoul, South Korea.
E-mail address: yryu@snu.ac.kr (Y. Ryu).

https://doi.org/10.1016/j.rse.2023.113696
Received 9 January 2023; Received in revised form 10 May 2023; Accepted 21 June 2023
Available online 4 July 2023

on limits imposed by either water or energy availability. The tight coupling between ecosystem carbon assimilation and water consumption implies that hydrologic factors limit the amount of carbon that can be fixed by ecosystems (Gentine et al., 2019; Law et al., 2002), and photosynthesis and transpiration are coupled via plant stomata (Baldocchi and Meyers, 1998; Leuning et al., 1995b). Terrestrial ecosystem respiration (TER) is a large, relatively conserved fraction (~0.8) of gross primary productivity (GPP), also referred to as CUE, in an undisturbed ecosystem (Baldocchi, 2008; Janssens et al., 2001). Under unstressed conditions, peak LUE (the ratio of canopy photosynthesis to absorbed light) is on the order of ~2% at an annual scale (Baldocchi, 2020). However, there has been little effort to monitor these fluxes concurrently in remote sensing community.

A comprehensive view of the carbon–water–energy nexus will improve our understanding of the complex interactions in terrestrial ecosystems, as well as the accuracy of land–atmosphere flux estimates. With the recent advances in remote sensing, emerging efforts have been meanwhile devoted to estimate carbon-water-energy fluxes in a coupled manner. Yuan et al. (2010) revised the Penman–Monteith equation to estimate ET independently, and then used ET-based water stress to quantify GPP using an LUE model. Zhang et al. (2016) developed a coupled carbon-centric model that first calculated GPP using LUE theory and then derived ET based on WUE (the ratio of canopy GPP to ET). Direct concurrent estimation of global transpiration and GPP has become feasible with the availability of satellite SIF data (Maes et al., 2020; Shan et al., 2021). Migliavacca et al. (2011) proposed a photosynthesis-dependent TER model by including GPP in the parameterization of the reference respiration rate. Keenan et al. (2016) later estimated global TER in a diagnostic model via the photosynthesis-dependent TER module. Other than that, process-based diagnostic models mechanistically represent underlying interactions between the biosphere and atmosphere, allowing simultaneous carbon–water–energy flux modeling (Chen et al., 1999; Ryu et al., 2011). To date, these coupled models have shown some improvements over other individual models.

Although such integrated flux models represent a significant step in simultaneous monitoring of terrestrial carbon–water–energy dynamics, they only partly incorporate coupled land–atmosphere fluxes. Even more single-flux products have been developed individually (Jung et al., 2020; Mu et al., 2011; Running et al., 2004). Thus, it remains difficult to obtain a complete picture of the behavior of terrestrial carbon, water, and energy cycles simultaneously, as well as their underlying processes. Uncoupled schemes may overlook key dynamics of essential land biophysical processes (Maxwell and Miller, 2005), and using different forcing data for individual flux models may lead to internal inconsistencies between carbon, water, and energy flux estimates, potentially causing substantial biases in global annual flux budgets (Yang et al., 2020). More importantly, the use of individual flux products can result in significant biases in estimating ecosystem functional properties; moreover, most remote-sensing-based land-surface flux products have been assessed only through direct evaluation against eddy covariance (EC) flux tower observations (Jiang and Ryu, 2016; Tramontana et al., 2016), and few attempts have been made towards more elaborate evaluations of the underlying functional properties.

At present, satellite records exceed 40 years of data and diverse EC studies have been conducted for longer than a decade. Long-term EC measurements (i.e., FLUXNET network data) have served as a backbone for ecosystem model development, calibration and validation (Chu et al., 2017; Jung et al., 2020; Migliavacca et al., 2011; Yuan et al., 2011). These measurements produce information on the functional properties of ecosystems, such as the Budyko relation and upper bounds on resource-use efficiency variables (Baldocchi and Penuelas, 2019). In turn, long-term remote-sensing observations have dramatically reshaped research approaches to the study of terrestrial ecosystem cycles worldwide through the integration of flux-tower and multi-source satellite data (Baldocchi et al., 2016; Ryu et al., 2019). However, long-term, remote-sensing-based, intra-consistent coupled flux maps remain rare on global scales.

The Breathing Earth System Simulator (BESS) is a remote-sensing-driven, process-based model that integrates key physical and biochemical processes related to land–atmosphere flux exchange (Jiang and Ryu, 2016; Ryu et al., 2011; Ryu et al., 2018). BESS has shown robust performance across temporal and spatial scales for the period 2000–2015. In this study, building on the previous framework of BESSv1.0 (Jiang and Ryu, 2016), we present a significantly improved version of the BESS model (BESSv2.0) that coherently integrates atmosphere and canopy radiative transfer, photosynthesis, ecosystem respiration and ET processes. New features in the new version of the BESS model include a new ecosystem respiration module that incorporates both photosynthesis and water availability, and a new maximum carboxylation rate (V_{cmax}) module based on an optimality principle (Jiang et al., 2020; Smith et al., 2019). The primary objectives of this study were to quantify long-term (1982–2019) daily global energy (i.e., surface downwelling shortwave radiation (SW) and net radiation (R_{net})), carbon (i.e., GPP, TER, and net ecosystem exchange (NEE)), and water (ET) fluxes concurrently, and to comprehensively evaluate BESS energy, carbon, and water flux products against in-situ FLUXNET network measurements across multiple temporal scales, independent state-of-the-art remote sensing estimates, and functional properties and their upper bounds on the basis of FLUXNET observations. Finally, we used BESS and a suite of flux products to determine whether coupled land–atmosphere flux modeling can improve ecosystem functional property estimates.

2. Materials and methods

2.1. BESSv2.0 overview

The BESS framework was developed to quantify global land–atmosphere fluxes by coupling essential physical and biochemical processes over the global land surface. In this section, we briefly present the overall framework of BESS(v2.0) (Fig. 1). The initial step in the BESS framework is to compute the components of solar shortwave radiation. A two-leaf, two-stream canopy radiative transfer model (De Pury and Farquhar, 1997; Ryu et al., 2011) was used to calculate absorbed photosynthetically active radiation (PAR) and near-infrared (NIR) radiation in sunlit and shaded canopies. An optimality-based model was used to quantify the C3 plant maximum canopy carboxylation rate at a standardized temperature of 25 °C (V_{cmax}^{25C}) (Jiang et al., 2020; Wang et al., 2017a), and a plant functional type (PFT)-dependent look-up table (LUT) method was applied to determine the C4 plant V_{cmax}^{25C} (Jiang and Ryu, 2016). Next, a carbon–water–energy module integrated with a two-leaf longwave radiative transfer model (Kowalczyk et al., 2006), Farquhar–von Caemmerer–Berry (FvCB) photosynthesis model (Collatz et al., 1992; Farquhar et al., 1980), Ball–Berry stomatal conductance equation (Ball, 1988), and the quadratic Penman–Monteith and energy balance equations (Kyaw, 1987; Paw and Gao, 1988), was adopted to compute R_{net}, ET, and GPP for sunlit and shaded C3 and C4 plant canopies separately in an iterative manner. In each land grid cell, the sum of the relative proportions of C3 and C4 plants was computed to determine the desired flux quantity. Then, the derived instantaneous estimates of R_{net}, GPP, and ET during satellite overpass were temporally upscaled to daily sums using a sinusoidal function (Bisht et al., 2005) for R_{net} and a cosine function (Ryu et al., 2012) for GPP and ET. Finally, daily TER and NEE were simulated based on topsoil organic carbon (SOC) stocks, air temperature (T_a), ET, potential ET (PET), and GPP. Compared to the previous version of BESS (Jiang and Ryu, 2016), the updated framework 1) included a new TER module and NEE module as the difference between GPP and TER, 2) revised the LUT-based V_{cmax}^{25C} module into an optimality-based one, to more accurately determine the seasonality of C3 plant V_{cmax}^{25C} by combining coordination theory and least-cost hypothesis, and 3) extends datasets back to 1982 through comprehensive

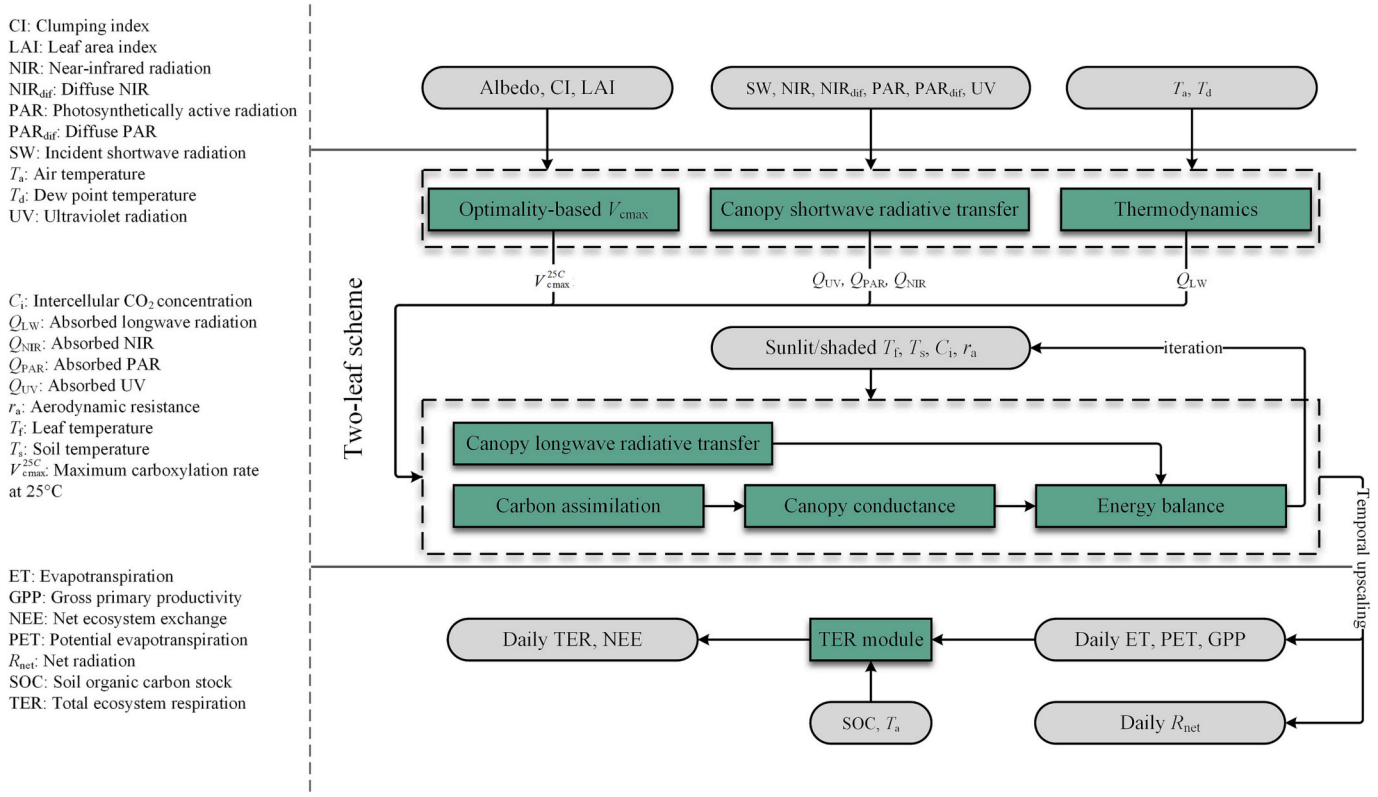

Fig. 1. Algorithm flowchart of the revised Breathing Earth System Simulator model (BESSv2.0). Gray ovals refer to the input/output variables. Green rectangles refer to the main modules. (For interpretation of the references to colour in this figure legend, the reader is referred to the web version of this article.)

calibration of Advanced Very High Resolution Radiometer (AVHRR) datasets using the MODerate Resolution Imaging Spectroradiometer (MODIS).

2.2. New schemes in BESS

2.2.1. TER module

To enable TER simulation in BESS, with the aim of constructing a fully-coupled model, we started from a widely used photosynthesis-dependent respiration model proposed by Migliavacca et al. (2011), which simulates TER in daily time steps using daily T_a and precipitation (P) as abiotic drivers, as follows:

$$TER = R_{ref} \times f(T_a) \times f(P) \quad (1)$$

where R_{ref} (g C m^{-2} d^{-1}) is ecosystem respiration at the reference temperature (T_{ref}, K) without water limitations, and $f(T_a)$ and $f(P)$ are the response functions of TER to T_a and P, respectively.

The carbon substrate availability in soil directly influences CO_2 emissions from microbial decomposition (Feng et al., 2018). Numerous studies have reported a strong linear relationship between SOC stocks and annual soil respiration (Bae and Ryu, 2017; Chen et al., 2010; Tao et al., 2016). To take the effect of the carbon substrate on TER into account, we included SOC stock as an additional biotic driver of R_{ref}, as follows:

$$R_{ref} = a_0 + a_1 SOC + a_2 GPP \quad (2)$$

A growing body of evidence has indicated the necessity of using mean annual temperature as T_{ref} for soil or ecosystem respiration estimation (Jian et al., 2020; Yuan et al., 2011). Therefore, instead of using a global constant T_{ref} for the Arrhenius-type $f(T_a)$ (Lloyd and Taylor, 1994), we calculated PFT-dependent T_{ref} based on the mean annual T_a from the FLUXNET2015 dataset (Table S1), as follows:

$$f(T_a) = e^{E_0\left(\frac{1}{T_{ref}-T_0}-\frac{1}{T_a-T_0}\right)} \quad (3)$$

where E_0(K) is the activation energy parameter and represents the ecosystem respiration sensitivity to temperature and T_0 is fixed at 227.13 K (−46.02 °C).

Although soil water content is widely regarded as an ideal descriptor of soil water availability, Migliavacca et al. (2011) adopted a precipitation-based soil water stress function—$f(P)$ because global soil water maps usually cover top soils at coarse spatial resolution. However, precipitation and soil water content are not tightly coupled, especially in forest sites (Migliavacca et al., 2015). Additionally, the monotonic increasing function [(Eq. 3 in Migliavacca et al. (2011)] ignored the negative effect on TER when soils are too wet (Baldocchi et al., 2018; Moyano et al., 2013). Given these findings, we replaced P with the ratio of ET to PET (fET), which is more directly related to soil water availability (Stocker et al., 2018). Then, we reformulated the soil water stress function as an exponential function with a quadratic expression that approaches 1 at the optimal fET (fET$_{opt}$) for TER release, as follows:

$$f(fET) = \beta^{\left(fET_{opt}-fET\right)^2} \quad (4)$$

where β is a free parameter (ranging from 0 to 1) that modifies the shape of the quadratic fit. The final formulation of the BESS-TER model is as follows:

$$TER = (a_0 + a_1 SOC + a_2 GPP) \times e^{E_0\left(\frac{1}{T_{ref}-T_0}-\frac{1}{T_a-T_0}\right)} \times \beta^{\left(fET_{opt}-fET\right)^2} \quad (5)$$

Based on the FLUXNET database (see Section 2.4.2), the TER model parameters were estimated using an adaptive Markov Chain Monte Carlo (MCMC) method (Haario et al., 2006; Haario et al., 2001). In this study, we used the 'MCMCSTAT' package (https://mjlaine.github.io/

mcmcstat/) to implement the MCMC simulation. We defined the cost function as the residual sum of squares in the TER model. Following the model calibration steps provided in Migliavacca et al. (2011), the three free R_{ref} parameters (a_0, a_1, a_2) were first estimated for each PFT and the accuracy of the linear model was evaluated. These parameters were then introduced as fixed parameters to obtain the remaining PFT-specific model parameters (E_0, β, and $f\mathrm{ET}_{opt}$) of the BESS-TER model. To generalize the model parameterization, we used all available data for each PFT in parameters fitting at the same time.

We adopted a 10-fold cross-validation scheme to evaluate the performance of the BESS-TER model (Schaffer, 1993). For each PFT, the whole dataset was stratified into 10 randomly selected subsets. In each cycle, 90% of the available sites were used to fit the model and the remaining 10% were used for validation. Each site was used only once for validation and the parameters were never evaluated against sites used for parameter calibration. For each PFT, we averaged the 10 sets of cross-validated statistics as a final single estimation of model accuracy. A detailed description of the TER model development is provided in the Supplementary Material.

2.2.2. V_{cmax} module

In the previous BESS version (Jiang and Ryu, 2016), the peak V_{cmax}^{25C} values of a pixel in each year were set as constants using an LUT based on PFTs and climatic zones, and their seasonal patterns were assumed to be empirical linear functions of seasonal leaf area index (LAI) trajectories. This parameterization ignored spatial variation within PFTs and interannual variations that could result in inaccurate carbon flux estimates. Therefore, we adopted a coordination theory and a least-cost hypothesis to estimate V_{cmax}^{25C} instead of the LUT approach (Jiang et al., 2020). The coordination theory states that plants adjust V_{cmax} to coordinate two key processes, the Calvin–Benson–Bassham cycle and light-dependent electron transport(Walker et al., 2017). Within the framework of the steady-state FvCB model, the carboxylation-limited photosynthesis rate (A_c) is equal to the electron transport-limited photosynthesis rate (A_j) under typical daytime environmental conditions during the past month (Wang et al., 2017a), as follows:

$$A_c = V_{cmax}\frac{C_i - \Gamma^*}{C_i + K} = A_j = \frac{\varphi_0 I}{4\sqrt{1+\left(\frac{aI}{J_{max}}\right)^2}}\frac{C_i - \Gamma^*}{(C_i + 2\Gamma^*)} \quad (6)$$

where C_i (Pa) is the intercellular CO_2 partial pressure, Γ_* (Pa) is the CO_2 compensation point in the absence of dark respiration, K (Pa) is the Michaelis–Menten coefficient for Rubisco-limited photosynthesis, φ_0 (g C/mol) is the intrinsic quantum yield of photosynthesis based on incident light, I (mol m^{-2} day^{-1}) is the incident PAR, and J_{max} (μmol m^{-2} s^{-1}) is the maximum electron transport rate. The optimality algorithm further assumes an optimal J_{max} that maximizes differences between the benefit (A_j) and cost ($c \times J_{max}$). Thus, the plant-averaged V_{cmax} can be obtained as follows (Jiang et al., 2020):

$$V_{cmax} = \varphi_0 I\frac{C_i - \Gamma^*}{C_i + 2\Gamma^*}\sqrt{1-\left[\frac{4c(C_i+2\Gamma^*)}{C_i-\Gamma^*}\right]^{\frac{2}{3}}} \quad (7)$$

We calculated Γ_* according to Bernacchi et al. (2001), and adopted the unit cost $c = 0.103$ by taking the typical value of $J_{max}/V_{max} = 1.88$ (Kattge and Knorr, 2007). The retrieval of φ_0 and C_i required several key variables including T_a, the vapor pressure deficit (VPD), ambient CO_2 partial pressure (C_a), the surface pressure (P_s) and the plant-level fraction of absorbed PAR (fPAR), which was estimated following Jiang et al. (2020). To account for the antecedent environment, we used 40-day backward running averaged values of *I*, T_a, *VPD*, C_a, P_s and fPAR as optimality-based model inputs (Jiang et al., 2020).

Next, we converted the plant-averaged V_{cmax} to top-leaf V_{cmax} ($V_{cmax,top\text{-}leaf}$) by accounting for vertical variation in leaf nitrogen content within the plant canopy (De Pury and Farquhar, 1997). We further converted $V_{cmax,top\text{-}leaf}$ to V_{cmax}^{25C} using an Arrhenius temperature function (Kattge and Knorr, 2007). Finally, we upscaled the leaf-level V_{cmax}^{25C} to sunlit/shaded canopy-level V_{cmax}^{25C} according to the method of Ryu et al. (2011). A detailed description of this optimality algorithm can be found elsewhere Jiang et al. (2020).

2.2.3. Stomatal conductance (g_s)

In the previous BESS model, plant carbon flux and water flux were coupled via the Ball–Berry stomatal conductance model. The slope (m) and intercept (b) parameter of the Ball-Berry model impact transpiration and photosynthesis estimates. The previous BESS version set constant Ball–Berry m and b parameters for C3 and C4 plants, respectively (Jiang and Ryu, 2016; Ryu et al., 2011), ignoring spatial and temporal variations. In BESSv2.0, we adopted an LUT method based on the literature (Table S3). We also developed a water stress scheme to downregulate minimum stomatal conductance (b_0), which becomes an important factor under very dry conditions.

We defined water stress (f_w) as a multiplicative factor (Fisher et al., 2008) for the initial Ball–Berry intercept b_0, then g_s was computed as follows:

$$g_s = m \times \frac{A_n \times RH}{C_a} + b \quad (8)$$

$$b = b_0 \times f_w \quad (9)$$

$$f_w = \mathrm{RH}^{\mathrm{VPD}/1000} \quad (10)$$

where A_n is the net CO_2 assimilation, b is the adjusted Ball–Berry intercept, and RH is the relative humidity of the air (ranging from 0 to 1).

2.3. Forcing datasets and preprocessing

The global-scale input datasets used for BESS are listed in Table 1. In total, BESS used seven MODIS atmosphere and land products (after 2001), two AVHRR land products (before 2000), four other satellite datasets, four reanalysis datasets, and four ancillary datasets as input data. All datasets were resampled to a 0.05° spatial resolution with geographic coordinates for global simulations. To minimize temporal inconsistencies between MODIS-derived (as a reference) and other gridded datasets such as AVHRR and reanalysis data, we conducted simple inter-calibrations based on ratios in terms of climatology (mean monthly values) for all datasets pixel by pixel over an overlapping period (2002–2017), except for land-cover and climate-classification maps. Fused long-term forcing datasets (1982–2019) were then generated for BESS.

2.3.1. Land surface datasets

LAI is the most important variable for BESS flux estimations (Huang et al., 2018; Ryu et al., 2011). We used MODIS and GLOBMAP LAI products to generate a long-term consistent LAI dataset. The MODIS MCD15A2H LAI product was used as input from January 2001 to June 2002 (Myneni et al., 2015a), whereas MCD15A3H LAI was used as input for the period after July 2002 (Myneni et al., 2015b) and GLOBMAP LAI was used as input for the period before January 2001 (Liu et al., 2012). Data from July 2002 to December 2017 were used to calibrate GLOBMAP LAI against MODIS LAI, and the resulting pixel-wise, 8-day interval parameters were applied to GLOBEMAP LAI. We applied a moving-window, threshold-based filtering algorithm to minimize cloud contamination effects on LAI estimates (Jiang and Ryu, 2016). Subsequently, data gaps in the filtered LAI were filled with monthly mean data, and further interpolated into daily data using a Gaussian function between contiguous data points.

Fractional vegetation cover (FVC) was mainly used to calculate $V_{cmax,top\text{-}leaf}$. We derived annual FVC for woody areas from the MOD44B

Table 1
Input data list for BESSv2.0 model. All the data were resampled to 0.05° for the flux simulations.

ID	Dataset	Temporal resolution	Spatial resolution	Satellite	Module
1	GMTED2010 global terrain elevation	One-off	1/120 °	Y	V_{cmax}; Energy balance;
2	Köppen-Geiger global climate classification	One-off	1/10 °	N	Canopy conductance
3	Global maize distribution	One-off	1/4 °	Y	V_{cmax}; Carbon assimilation;
4	Global C4 grass distribution	One-off	1/4 °	N	Carbon assimilation
5	Global forest canopy height	One-off	1/120 °	Y	Energy balance
6	Harmonized World Soil Database (HWSD)	One-off	1/120 °	N	TERTER
7	Soil organic carbon stock	One-off	250 m	Y	
8	Global canopy clumping index	Climatology	500 m	Y	Energy balance; Canopy shortwave radiative transfer; V_{cmax};
9	WorldClim wind speed data	Climatology	1/120 °	N	Thermodynamics
10	CCI global land cover classification	Annual	1/360 °	Y	
11	MCD12Q1 C6 land cover classification	Annual	500 m	Y	TER; Canopy conductance; Carbon assimilation;
12	VIPPHEN_EVI2 global phenology	Annual	5 km	Y	V_{cmax}
13	VPN22C2 global phenology	Annual	5 km	Y	
14	MEaSUREs vegetation continuous fields	Annual	5 km	Y	Energy balance
15	MOD44B vegetation continuous fields	Annual	250 m	Y	
16	OCO-2 Global carbon dioxide distribution	Monthly	1 °	Y	
17	GHG-CCI global carbon dioxide distribution	Monthly	5 °	Y	Canopy conductance
18	NOAA sites carbon dioxide measurements	Monthly	–	N	
19	GLOBMAP leaf area index	Half-monthly	1/13.75 °	Y	V_{cmax}; Canopy shortwave radiative transfer; Canopy longwave radiative transfer; Carbon assimilation; Energy balance;
20	MOD15A2H C6 leaf area index	8-day	500 m	Y	
21	MCD15A3H C6 leaf area index	4-day	500 m	Y	
22	GLASS black/white-sky shortwave albedo	8-day	1/20 °	Y	
23	MCD43D59 C6 black/white-sky visible albedo	Daily	1/120 °	Y	
24	MCD43D60 C6 black/white-sky near-infrared albedo	Daily	1/120 °	Y	
25	MCD43D61 C6 black/white-sky shortwave albedo	Daily	1/120 °	Y	Canopy shortwave radiative transfer
26	MOD04_L2 C6 aerosol	Daily	10 km	Y	
27	MYD04_L2 C6 aerosol	Daily	10 km	Y	BESS radiation
28	MOD06_L2 C6 cloud	Daily	1 km	Y	
29	MYD06_L2 C6 cloud	Daily	1 km	Y	
30	MOD07_L2 C6 atmospheric profiles	Daily	5 km	Y	BESS radiation; Thermodynamics; TER;
31	MYD07_L2 C6 atmospheric profiles	Daily	5 km	Y	
32	ERA5 solar radiation	Hourly	1/4 °	N	BESS radiation; Canopy shortwave radiative transfer;
33	ERA5 air temperature	Hourly	1/4 °	N	Thermodynamics; TER;
34	ERA5 dewpoint temperature	Hourly	1/4 °	N	Thermodynamics;

yearly 250-m Vegetation Continuous Fields (VCF) product after 2001 (Dimiceli et al., 2015), and the inter-calibrated MEaSUREs yearly 0.05° VCF product (VCF5KYR) for the period before 2000 (Hansen and Song, 2018), by assuming that woody plants have static canopy cover within a given year. For grasslands and croplands, we calculated dynamic FVC data using Beer's law in the nadir direction, as follows:

$$\mathrm{FVC} = 1 - e^{-0.5\Omega LAI} \tag{11}$$

We used MEaSUREs Vegetation Index and Phenology (VIP) global phenology data (VIPPHEN_EVI2) to determine the starting date and length of the growing season. Next, we converted the plant-averaged V_{cmax} to $V_{cmax,top\text{-}leaf}$, as follows:

$$V_{cmax,top-leaf} = V_{cmax}\frac{k_n}{1 - e^{-k_n}} \tag{12}$$

$$k_n = -0.53ln(LAI_{GS}) + 0.92 \tag{13}$$

where k_n is the nitrogen distribution coefficient, and LAI_{GS} is mean plant-level LAI (LAI_p) during the growing season, and LAI_p.can be given by:

$$LAI_p = LAI/FVC \tag{14}$$

Land-cover-type data from the MCD12C1 yearly product with the International Geosphere–Biosphere Programme (IGBP) scheme for the period 2001–2019 (Friedl and Sulla-Menashe, 2015), alongside the European Space Agency Climate Change Initiative (ESA-CCI) product (further converted into IGBP classes) for the period before 2001 (Defourny et al., 2012), were used to perform PFT-based parameterizations of the C4 fraction, canopy height, ball–berry m and b, and TER model parameters.

Canopy-height data were used to compute the aerodynamic resistance in the energy balance module. We used global canopy-height data derived from the Geoscience Laser Altimeter System (GLAS) LiDAR instrument onboard the NASA Ice, Cloud, and land Elevation (ICESat) satellite (Simard et al., 2011), which provides global forest-canopy-height estimates at 30-s spatial resolution. Although the dataset represents only a single year (2005), we used it for the entire BESS time period (1982–2019) due to a lack of dynamic data. Non-forest and C4 plant land-cover areas were set to 1- and 2-m height, respectively, based on annual land-cover maps.

Visible and NIR albedo products were used to simulate canopy shortwave radiative transfer in BESS v2.0, following Jiang and Ryu (2016). Shortwave albedo products were used to compute incoming solar radiation and surface net radiation in BESS. For the period after 2001, we used MODIS MCD43D59, MCD43D60, and MCD43D61 black-

and white-sky albedo products for visible, NIR, and shortwave broadband wavelengths, respectively. For the period before 2000, we used Global Land Surface Satellite (GLASS) black- and white-sky albedo products.

MODIS albedo products apply a rolling-weight strategy to derive daily albedo using 16-day surface-reflectance data acquired by the Terra and Aqua satellites, with a spatial resolution of 30 s. We excluded pixels as outliers if their daily albedo values were beyond the monthly mean ± 2 monthly standard deviations (SD). Subsequently, data gaps in daily albedo were filled with monthly data. The GLASS albedo product provides 0.05° albedo at 8-day intervals. We applied the same procedure for pixel-wise inter-calibration with MODIS data. The resulting 8-day data were linearly interpolated into daily intervals.

2.3.2. Climate datasets

Daily 2-m air temperature (T_a) and dew point temperature (T_d) data were derived from ERA5 products (Hersbach et al., 2018). Standard ERA5 data were provided at 0.25° × 0.25° resolution and 1-h intervals. To match the BESS spatial resolution (0.05°), we performed spatial downscaling on original ERA5 air-temperature data using WorldClim climatology data (1-km resolution, aggregated to 0.05°; http://worldclim.org/version2) and MODIS monthly mean T_a and T_d derived from the MOD07/MYD07_L2 product (5-km resolution) as proxies for the periods before 2000 and after 2001, respectively. Pixel-wise ratios of coarse-scale ERA-derived temperatures to 0.05° temperature were used as a downscaling factor to compute fine-scale ERA-derived temperature datasets. The downscaling formula is given as:

$$X_{fine} = R_{fine} \times C_{fine} \tag{15}$$

$$C_{coarse} = X_{coarse} / R_{coarse} \tag{16}$$

where X and R are the target and reference datasets, respectively; C is the downscaling coefficient; the fine and coarse subscripts indicate the resolution level, X_{fine}, X_{coarse}, and R_{fine} are the downscaled ERA5, original ERA5, and MODIS-derived data, respectively; and R_{fine} was aggregated into R_{coarse} by averaging fine-resolution data within each coarse-resolution grid. To avoid boundary effects, we linearly interpolated C_{coarse} into C_{fine}, rather than direct substitution.

For the MODIS period after 2001, we adopted solar-radiation data from BESS (BESS-Rad). BESS-Rad computes solar radiation components, including surface downwelling shortwave radiation (SW), ultraviolet radiation, direct PAR, diffuse PAR, direct NIR radiation, and diffuse NIR radiation through synergistic application of the Forest Light Environmental Simulator (FLiES) and an artificial neural network (Ryu et al., 2018). We used ERA5 SW data (Hersbach et al., 2018) to obtain radiation components before 2000 using an empirical method (Weiss and Norman, 1985) and computed ultraviolet radiation by assuming a 5% proportional relationship with SW (IARC Working Group on the Evaluation of Carcinogenic Risks to Humans. Radiation. Lyon FR; International Agency for Research on Cancer, 2012). We applied the same procedures to further downscale and inter-calibrate these variables and fill data gaps within the MODIS period using ERA5-derived data.

The Orbiting Carbon Observatory-2 (OCO-2) Lite Version-7 XCO_2 product for 2015 (oco2.gesdisc.eosdis.nasa.gov) and National Oceanic and Atmospheric Administration (NOAA) Annual Mean Global Carbon Dioxide Growth Rates data (www.esrl.noaa.gov/gmd/ccgg/trends/) were harmonized to generate spatiotemporally varying ambient CO_2 concentration maps at 0.05° resolution from 1982 to 2019.

National Centers for Environmental Prediction (NCEP)/ National Center for Atmospheric Research (NCAR) Reanalysis wind speed data (www.esrl.noaa.gov/psd/data/gridded/) (Kalnay et al., 1996) were used in the aerodynamic module.

The Tropical Rainfall Measuring Mission (TRMM) 3B43 v7 precipitation data were used in the Budyko relation evaluation at the global scale (Huffman et al., 2007). We used the Global Land Data Assimilation System (GLDAS-Noah) v2.1 precipitation data (Rodell et al., 2004) to fill gaps in daily TRMM data, and then resampled the gap-filled precipitation data to 0.05° resolution using the nearest neighborhood method.

2.3.3. Ancillary datasets

SOC stock data were downloaded from the SoilGrids system (https://www.soilgrids.org) generated at the International Soil Reference and Information Centre (Hengl et al., 2017). SoilGrids v2.0 (Batjes et al., 2020), with a resolution of 250 m, is currently the most detailed global soil dataset, acquired with high accuracy (Dai et al., 2019). We used topsoil SOC stock (0–15 cm) as the input data for TER model development.

To account for the spatial distribution of foliage in acquiring the sunlit fraction of canopy and FVC, we used a global 500-m, 8-day clumping index (CI) product derived from MODIS data (Wei et al., 2019). To reduce data noise and gaps, we computed mean monthly CI maps for 2001–2017 on a global scale, and used these for BESS simulations of the entire time period.

We used the five main climate groups (tropical, dry, temperate, continental, and polar) of the Köppen-Geiger climate classification map (Peel et al., 2007) in data-gap-filling procedures and Ball–Berry m parameterization.

Using the MsTMIP maize-fraction map (Monfreda et al., 2008) and C4 grass-relative-fraction ($F_{C4,r}$) map (Still et al., 2003), BESS computes GPP, ET, and R_{net} for C3 and C4 plants separately in a grid cell. The MsTMIP datasets provide estimates of the percentage of each grid cell covered by maize and the relative percentage covered by C4 grass over the globe. Although these datasets represent only a single year (ca. 2000), we used them for the entire BESS time period (1982–2019) due to a lack of dynamic data. Annual tree cover (F_{Tree}) was also obtained from MOD44B yearly VCF product. Due to the significant discrepancy between VCF5KYR and MOD44B tree cover data, we used MOD44B F_{Tree} of 2000 as a static model input for the period before 2000. We further generated an annual C4 grass fraction (F_{C4}) map by combining annual land-cover, tree-cover and C4 relative-fraction maps:

$$F_{C4} = \begin{cases} (1 - F_{Tree}) \times F_{C4,r}, \text{for savannas and woody savannas} \\ F_{C4,r}, \text{for grasslands} \end{cases} \tag{17}$$

The Shuttle Radar Topography Mission (SRTM) global 30-arcsec elevation product (Jarvis et al., 2008) was used to consider the effect of elevation on incoming radiation.

2.4. Datasets for model evaluation and calibration

2.4.1. Global-scale land–atmosphere datasets

At global level, we performed a comprehensive intercomparison between BESS and 18 other long-term gridded land–atmosphere flux products (using three machine-learning methods, three LUE models, 10 dynamic global vegetation models (DGVMs), and one reanalysis product), in terms of global total values and/or mean annual sum patterns.

FLUXCOM datasets are commonly used as benchmark or reference data in global carbon- and water-cycle studies (Bastos et al., 2020; Ryu et al., 2019; Tagesson et al., 2021). FLUXCOM products have provided ensemble R_{net}, LE, GPP, TER, and NEE values derived using three machine-learning methods, at 0.5° spatial resolution since 1979 (RS + METEO setup; i.e., remote-sensing and meteorology) and at 0.0833° spatial resolution since 2001 (RS setup) (Jung et al., 2020). We used the RS + METEO dataset to intercompare long-term global total flux estimates, and the RS dataset for site-level evaluation and intercomparison of spatial patterns, due to its higher spatial resolution. LUE-based global GPP estimates were obtained using P (Stocker et al., 2020), light response function (LRF) (Tagesson et al., 2021), and photosynthesis–respiration (PR) models (Keenan et al., 2016). Among these, the PR model couples a semi-empirical TER model based on Migliavacca et al. (2011) and EC data. We also used an ensemble of global

simulations of 10 DGVMs from the Trends in Net Land-Atmosphere Exchange (TRENDY-v1) project (Sitch et al., 2015) to benchmark GPP, TER, and NEE estimates concurrently. For ET data comparison, we included products derived from two process-based models, Process-based Land Surface evapotranspiration/Heat flux (P-LSH) (Zhang et al., 2010; Zhang et al., 2015) and the Global Land Evaporation Amsterdam Model (GLEAM) (Martens et al., 2017; Miralles et al., 2011). All map-to-map intercomparisons were made at an annual step and 0.5° resolution for the overlapped time span of each flux product.

2.4.2. FLUXNET datasets

We used the entire recently released FLUXNET2015 Tier 1 dataset, covering a total of 206 flux sites and 1496 site-years (Pastorello et al., 2020), for model calibration and validation. We used daily GPP and TER reference data obtained using the daytime partitioning method (i.e., GPP_DT_CUT_REF and RECO_DT_CUT_REF), and consolidated T_a (i.e., TA_F) from gap-filled T_a, gap-filled LE (i.e., LE_F_MDS) and R_{net} (i.e., NETRAD). All data were further filtered using data-quality flags at a threshold of >0.8, based on a fraction from 0 to 1 indicating the proportion of measured and good-quality gap-filled data. We further calculated PET according to Priestley and Taylor (1972).

The research sites included in the FLUXNET2015 Tier 1 dataset cover 11 major PFTs defined by the IGBP from tropical to arctic climate zones, including 15 evergreen broadleaf forests (EBF), 26 deciduous broadleaf forests (DBF), 10 mixed forests (MF), 49 evergreen needleleaf forests (ENF), six woody savannas (WSA), eight savannas (SAV), two closed shrublands (CSH), 12 open shrublands (OSH), 37 grasslands (GRA), 20 croplands (CRO), and 20 wetlands (WET). Due to the limited numbers of sites and the similarities among them, we combined both open (OSH) and closed (CSH) shrublands sites into one shrublands class (SHB).

Site-level evaluation of BESS flux products was performed based on five error metrics, the coefficient of determination (R^2), root mean square error (RMSE), normalized root mean square error (NRMSE, RMSE normalized (divided) by the magnitude of observed variability (standard deviation)) (Keenan et al., 2012), mean bias error (Bias), and relative mean bias error (Rbias, the difference between estimated and observed values divided by the observed mean). We further evaluated BESS performance according to ecosystem functional properties that learned from FLUXNET measurements, including the Budyko relation, CUE, WUE and LUE.

2.5. Evaluations of ecosystem functional properties

2.5.1. The Budyko equation

The Budyko relation implies a functional property between long-term-average ET and water and energy balance in large watersheds (Williams et al., 2012). We solved for the best-fit curve using mean annual values from both FLUXNET and satellite datasets, to demonstrate the physical principles of water and energy availability governing water balance through the Budyko space (evaporative index (= ET/P) vs. dryness index (= PET/P)), as follows:

$$\frac{ET}{P} = \frac{1}{\left(1 + (P/PET)^n\right)^{1/n}} \tag{18}$$

where n is the curvature parameter of the best-fit curve.

2.5.2. CUE

CUE can be defined as either the ratio between mean annual TER and GPP (definition 1), or the slope of the regression between TER and GPP (definition 2). Recent investigations suggest a CUE of ~0.8 using both approaches based on global observational datasets (Baldocchi, 2020). Hence, we comprehensively used definition 1 for global-level CUE evaluations (see Section 3.1 and 3.3), and used both definitions for site-level CUE evaluations (see Section 3.4).

3. Results

3.1. Global annual carbon and energy budgets

BESS estimates for global mean annual total carbon, water, and energy fluxes over land surfaces from 1982 to 2019, along with corresponding functional properties, are summarized in Fig. 2. As the ultimate energy input, SW exceeded all other energy components by at least two times of magnitude. On an annual scale, multiple environmental and physiological constraints lowered the SW energy committed towards GPP by 858.97 ZJ yr^{-1} (zetta = 10^{21}), leading to a final LUE (i.e., GPP/absorbed PAR (APAR), with an energy–quanta conversion factor of 4.56) of 1.50%. Approximately 87% of the GPP was subsequently respired back into the atmosphere through heterotrophs and autotrophs. A total of 67.67 × 10^3 km^3 yr^{-1} of water was consumed to fix 125.74 Pg C yr^{-1}, indicating a WUE of 1.86 g C kg^{-1}-H_2O.

3.2. Site-level evaluation of BESS against FLUXNET observations

3.2.1. Overall accuracy

Site-level BESS evaluation results are provided in Table 2. Overall, both daily and monthly 1-km BESS fluxes agreed well with FLUXNET measurements. Average R^2 values ranged from 0.31 (NEE) to 0.84 (R_{net}), and the relative bias varied from −1% (R_{net}) to 80% (NEE) at the daily scale. BESS flux estimate performance was generally better at the monthly scale, explaining 40% (NEE) to 92% (R_{net}) of variation. Except for NEE, the BESS model explained more than half of all interannual variation in FLUXNET measurements over all sites, with a relative bias of −19% (GPP) to −1% (R_{net}). However, the model captured only 13% of the interannual variation in NEE, and exhibited systematic overestimation of NEE (Rbias = 69%).

3.2.2. Comparison with benchmark products

We further evaluated the performance of BESS in comparison with two benchmark products, FLUXCOM and GLASS, at a monthly step against FLUXNET tower pixels (Fig. 3). All three products were resampled to a 0.05° spatial resolution. Overall, all three products agreed well with FLUXNET observations. For energy flux estimates, FLUXCOM had a higher R^2 and lower RMSE and Bias than the other two products. For LE estimates, BESS showed a small underestimation (Rbias = −4%), whereas GLASS tended to overestimate LE to some extent (Rbias = 38%). By contrast, the carbon flux estimates of all three products had similar R^2 values. For GPP estimates, BESS and GLASS performed better in terms of RMSE and Bias than FLUXCOM, which consistently underestimated GPP in months with high values.

3.3. Global intercomparison with benchmark datasets

3.3.1. Global total coupled flux budgets

At the global scale, there were distinct differences in the magnitudes or trends of total flux estimates from various models (Fig. 4). A comparison of diverse land-surface flux products showed that global BESS annual flux estimates were generally within or close to the most plausible ranges (Table S4). FLUXCOM estimated all fluxes with smaller interannual variability. Most of the other annual global GPP and TER estimates yielded similar upward trends, but with large variations in magnitude between estimates. An ensemble of 10 dynamic global vegetation models for the TRENDY datasets showed large uncertainties, exceeding 10 Pg C yr^{-1} in both global GPP and TER estimates. By contrast, larger divergences were found among the functional properties of fluxes. Specifically, BESS WUE showed a clear increasing trend (0.009 g C kg^{-1} yr^{-2}), whereas FLUXCOM and GLASS WUE were more conservative, showing lower magnitudes. For CUE, BESS, PR, and TRENDY showed slight decreasing trends, unlike FLUXCOM. GLASS exhibited no substantial trend in LUE, whereas BESS showed a strong increasing trend (0.005% yr^{-2}), with lower magnitudes since 1982.

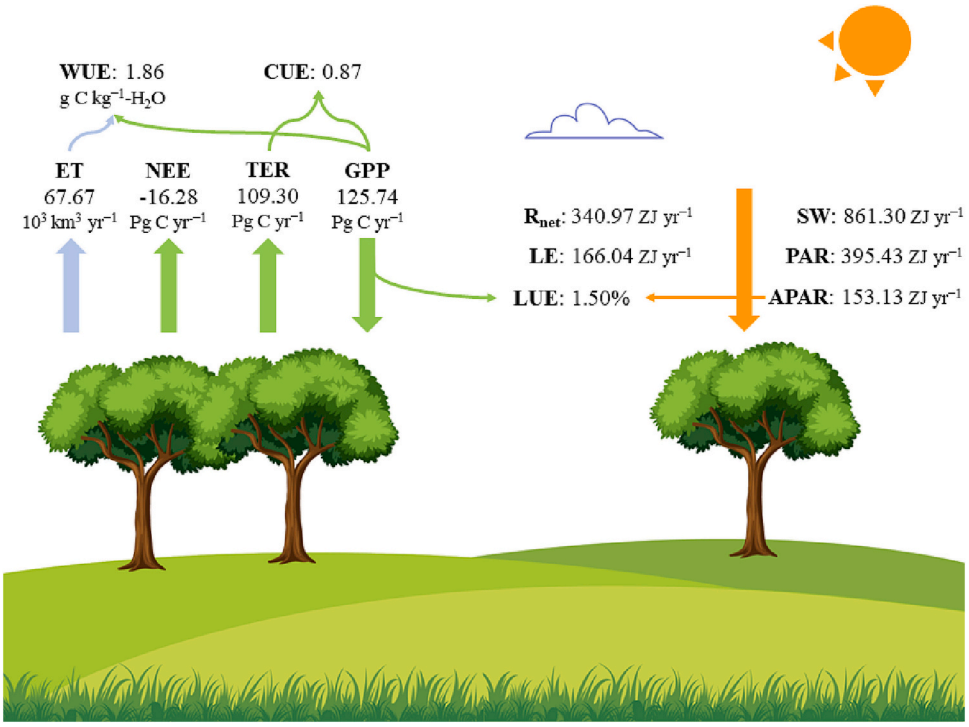

Fig. 2. BESS estimates of mean annual total carbon, water and energy balance components over land from 1982 to 2019. Some background graphics were downloaded from https://www.vecteezy.com/.

Table 2
Evaluation of BESS performance compared with FLUXNET observations. Error metrics were calculated based on 1-km-resolution forcing data. NRMSE and Rbias values are given in brackets.

Flux	Daily			Monthly			Annual		
	R^2	RMSE	Bias	R^2	RMSE	Bias	R^2	RMSE	Bias
GPP[a]	0.65	2.56(62%)	−0.69(−19%)	0.73	2.12(55%)	−0.68(−18%)	0.67	477.23(72%)	−255.60(−19%)
TER[a]	0.51	2.02(72%)	−0.05(−2%)	0.65	1.53(61%)	−0.07(−2%)	0.61	358.14(63%)	−40.68(−4%)
NEE[a]	0.31	2.22(87%)	0.59(80%)	0.40	1.78(83%)	0.59(78%)	0.13	306.41(122%)	147.85(69%)
LE[b]	0.53	2.31(71%)	−0.12(−3%)	0.65	1.75(61%)	−0.13(−4%)	0.51	427.79(72%)	−49.70(−4%)
R_{net}[b]	0.84	2.46(42%)	−0.07(−1%)	0.92	1.69(33%)	−0.09(−1%)	0.73	423.51(54%)	−35.36(−1%)

[a] The units of RMSE and Bias are g C m^{-2} d^{-1}, g C m^{-2} d^{-1}, and g C m^{-2} yr^{-1} at daily, monthly and annual time scales, respectively.
[b] The units of RMSE and Bias are MJ m^{-2} d^{-1}, MJ m^{-2} d^{-1}, and MJ m^{-2} yr^{-1} at daily, monthly and annual time scales, respectively.

3.3.2. *Spatial patterns of mean annual sum values*

The global spatial distributions of BESS mean annual fluxes and functional properties from 1982 to 2019 are shown in Fig. 5. Overall, the patterns of mean annual GPP, TER, and ET were similar, with hotspots occurring in densely vegetated tropical regions (Fig. 5), where evergreen broadleaf forests dominate between 20°N and 20°S. The southeast side of Asia, North America, and Oceania generally had higher GPP, TER, and ET, corresponding to humid subtropical climates. Small GPP, TER, and ET fluxes were mainly observed in cold and dry regions (e.g., central Eurasia and the Arctic). Mean annual R_{net} exhibited a dominant gradient between high values in the tropics and low values at high latitudes. By contrast, BESS mean annual NEE values indicated sizable carbon sinks across most croplands and forests, except for tropical forests in Amazon and Africa, and small carbon sources in drylands globally. The spatial distribution of CUE was comparable to that of NEE, and WUE and LUE showed similar overall patterns. Croplands and tropical forests had higher WUE and LUE than other PFTs.

There were considerable regional disparities among FLUXNET, BESS, and GLASS datasets across land–atmosphere fluxes and functional properties (Fig. S2 and S3). In particular, BESS showed consistently lower R_{net} and ET values than FLUXCOM across all tropical regions, whereas the opposite was the case for most dry and cold regions. Over most croplands worldwide, BESS yielded higher GPP and TER values than FLUXCOM, with slightly lower values in south central Asia, northern North America, and southern South America. BESS showed higher TER estimates in the Amazonian and African rain forests. FLUXCOM NEE differed notably from BESS NEE, which showed a more heterogeneous pattern (Fig. S2). For example, in tropical evergreen broadleaf forests, BESS NEE demonstrated carbon neutrality (Fig. 5), whereas FLUXCOM tended to show a strong carbon sink. The distribution pattern of CUE differences between BESS and FLUXCOM was comparable to that of NEE differences. For WUE, BESS generally showed larger values over regions dominated by C4 plants (especially croplands), whereas BESS agreed better with FLUXCOM in regions dominated by C3 plants. Similarly, GLASS showed lower GPP values than BESS over most croplands worldwide except in India, but higher GPP values over tropical evergreen forests (Fig. S3). GLASS consistently showed larger ET values than BESS in tropical evergreen forests, subtropical forests, and croplands, in patterns similar to those of FLUXCOM values, whereas opposite patterns were observed over the Tibetan Plateau; little difference in ET was observed in other locations. Overall, the spatial mismatch between BESS and GLASS ET was greater than that between BESS and FLUXCOM. Correspondingly, GLASS generated much larger WUE over most croplands compared to BESS. BESS exhibited

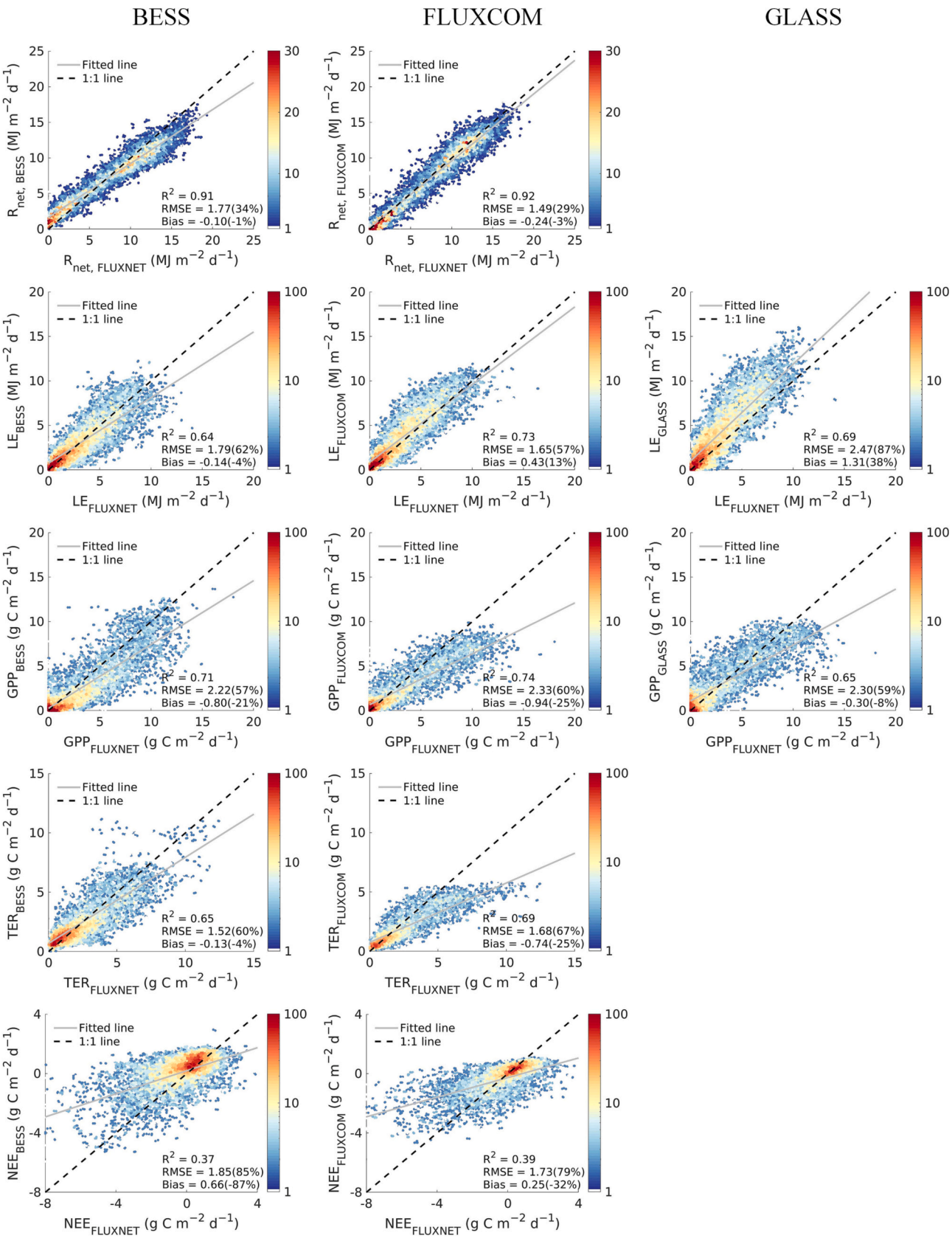

Fig. 3. Density scatterplots evaluating BESS (first column), FLUXCOM (second column), and Global Land Surface Satellite (GLASS) (third column) performance against EC observations at a monthly scale and 0.05° spatial resolution. NRMSE and Rbias values are given in brackets.

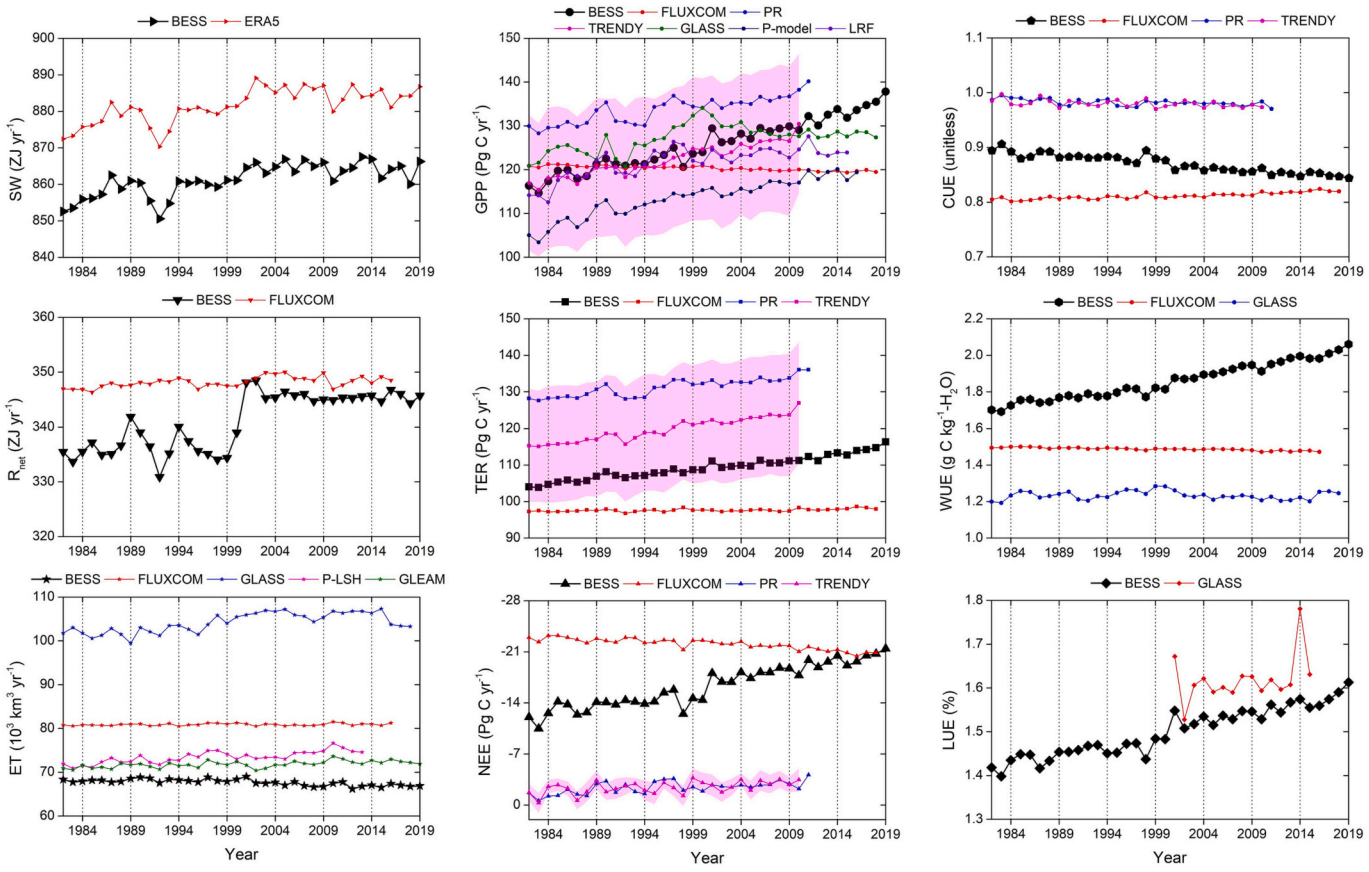

Fig. 4. Comparison of annual global total flux estimates from various models. The shaded pink area represents the interval of 1 standard deviation from 10 TRENDY models. (For interpretation of the references to colour in this figure legend, the reader is referred to the web version of this article.)

higher LUE values than GLASS over extratropical croplands and forests, as well as shrublands around the Arctic region. Despite these regional mismatches, the mean annual sums of BESS fluxes showed moderate consistency with both FLUXCOM ($R^2 \geq 0.77$ for all fluxes except for $R^2 = 0.32$ in NEE) and GLASS ($R^2 = 0.80$ and 0.85 for ET and GPP, respectively).

3.4. Evaluation of functional properties

3.4.1. Budyko relation

We evaluated the Budyko relation (evaporative index vs. dryness index) according to various remote-sensing products against direct measurements from the FLUXNET database. The Budyko relation relies on two fundamental physical limits (Fig. 6); first, that the demand limit implies that actual ET cannot surpass PET, and follows a 1:1 line (ET = PET), and second that the supply limit implies that actual ET cannot surpass water supply ($ET/P \leq 1$) in the absence of a substantial contribution by run-on or phreatic water sources. The best-fit curve of BESS estimates had a curvature parameter of $n = 1.58$, which was slightly lower than the measured FLUXNET value (1.80), whereas the FLUXCOM value was markedly higher (4.61). Most BESS estimates were below the demand and supply limits. By contrast, FLUXCOM estimates somewhat violated the functional constraints, with much more exceptions above the demand line (ET = PET) in the observed Budyko space (Fig. 6c). We also used whole global land pixels to fit the curvature parameter (Fig. 6d, e). There are more values above the supply line (ET = P) for both remote-sensing products and FLUXNET observations (ET > P, as shown in Fig. 6), especially among temperate and continental climate zone sites. More specifically, the fraction of values above the supply line in global FLUXCOM estimates (14.89%) was nearly twice that of BESS (7.62%). The largest deviations in BESS estimates were mainly located in arid climate regions, where ET is typically small.

3.4.2. CUE comparisons

The annual sums of GPP and TER appeared to be strongly coupled (Fig. 7). On average, 0.80, 0.71, and 0.77 of CUE (defined as the slope of the regression between TER and GPP) was obtained, and 86%, 95%, and 80% of the variance in TER was explained by variation in GPP based on the BESS, FLUXCOM and FLUXNET data, respectively. Similar results were observed from both BESS and FLUXCOM based on whole global land pixels (Fig. 7d, e). Notably, FLUXCOM showed very high linear relationships between GPP and TER ($R^2 = 0.95$ for FLUXNET sites, $R^2 = 0.99$ for global land pixels).

3.4.3. WUE comparisons

At the site scale, PFT-specific WUE (GPP vs. ET) estimates from BESS agreed better with FLUXNET measurements than those of GLASS and FLUXCOM (Figs. 8 and S4). Linear regression analysis showed that the fitted slopes of annual sum GPP and ET values obtained using BESS (slope = 0.27) were similar to those of FLUXNET WUE (slope = 0.23). By contrast, GLASS and FLUXCOM data showed larger slopes (~0.41), indicating that more water was used to fix carbon. On average, FLUXNET WUE observations for SHB (1.46 ± 0.83 g C kg^{-1}-H_2O) were found to be smaller than those of other PFTs, but were high for MF (3.59 ± 1.61 g C kg^{-1}-H_2O). By contrast, fitted intercepts were relatively conservative across site-level BESS, GLASS and FLUXCOM estimates and FLUXNET measurements.

Overall, global-level WUE derived from whole land pixels showed similar distributions to site-level values (Fig. 8a–c). There was tight coupling between GPP and ET across different satellite datasets and different spatial scales (from site to global level), despite all global-level plots presenting lower WUE than site-level plots. However, a clear

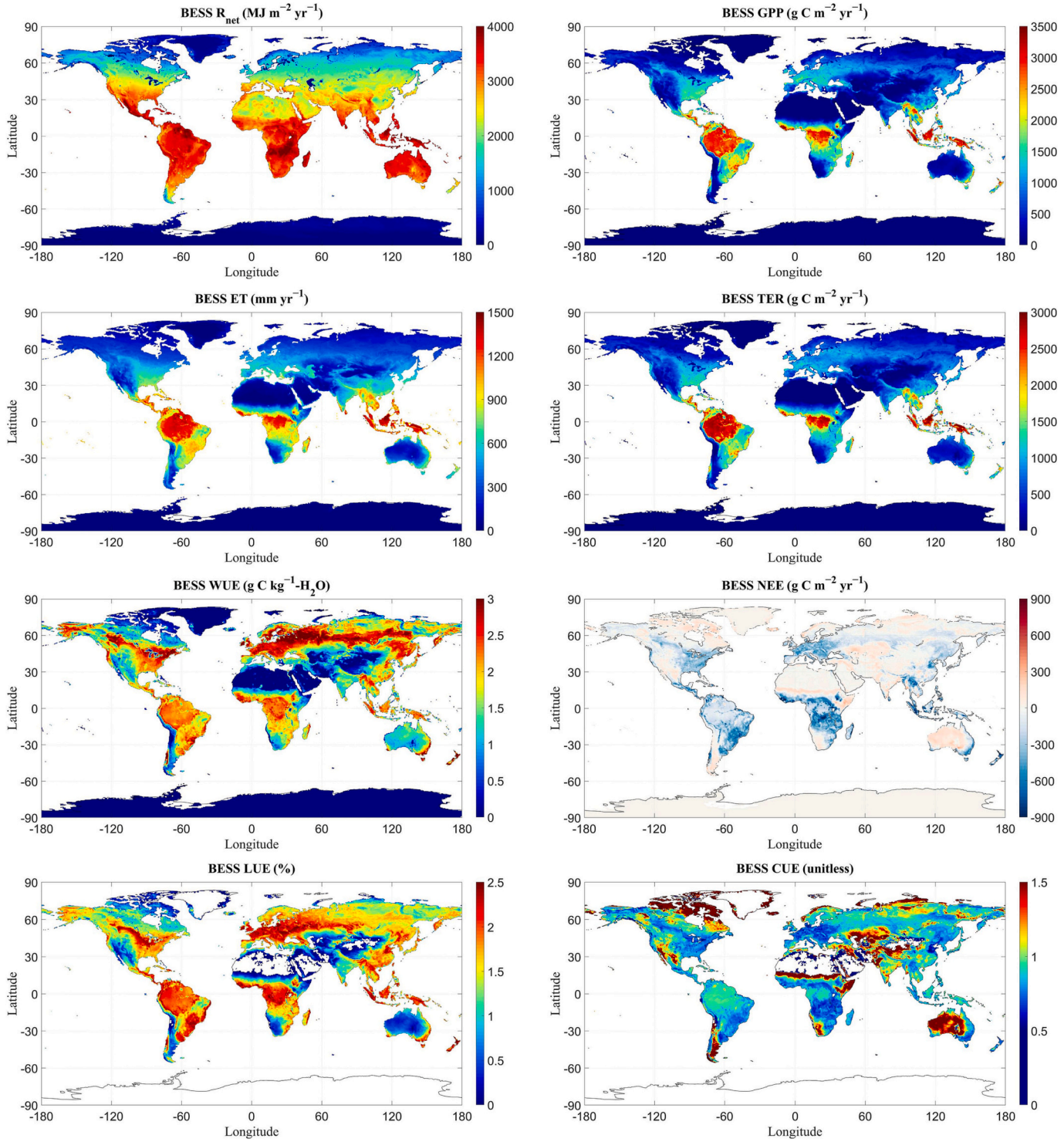

Fig. 5. BESS global mean annual fluxes and functional properties from 1982 to 2019. WUE = GPP/ET; LUE = GPP/APAR; CUE = TER/GPP.

saturation effect was also detected in FLUXCOM global estimates (Fig. 8g). On an annual basis, terrestrial ecosystems that assimilated >3000 g C m^{-2} yr^{-1} evaporated >1000 mm of water.

3.4.4. *LUE comparisons*

Site-level LUE (GPP vs. APAR) comparisons indicated similar patterns among the FLUXNET, BESS, and GLASS datasets, whereas global LUE from BESS was generally higher than that from GLASS (Figs. 9 and S5). Noted that the FLUXNET APAR was derived by multiplying measured PAR and MODIS fPAR, and the corresponding LUE pattern was slightly more scattered than those of the other two products. At both the site and global levels, scatterplots of APAR and GPP revealed that maximum LUE on the annual scale was approximately 2%, and actual LUE sometimes diverged from the maximum LUE under biotic and abiotic stress. EBF and CRO generally had higher LUE values than the other PFTs (Fig. 5).

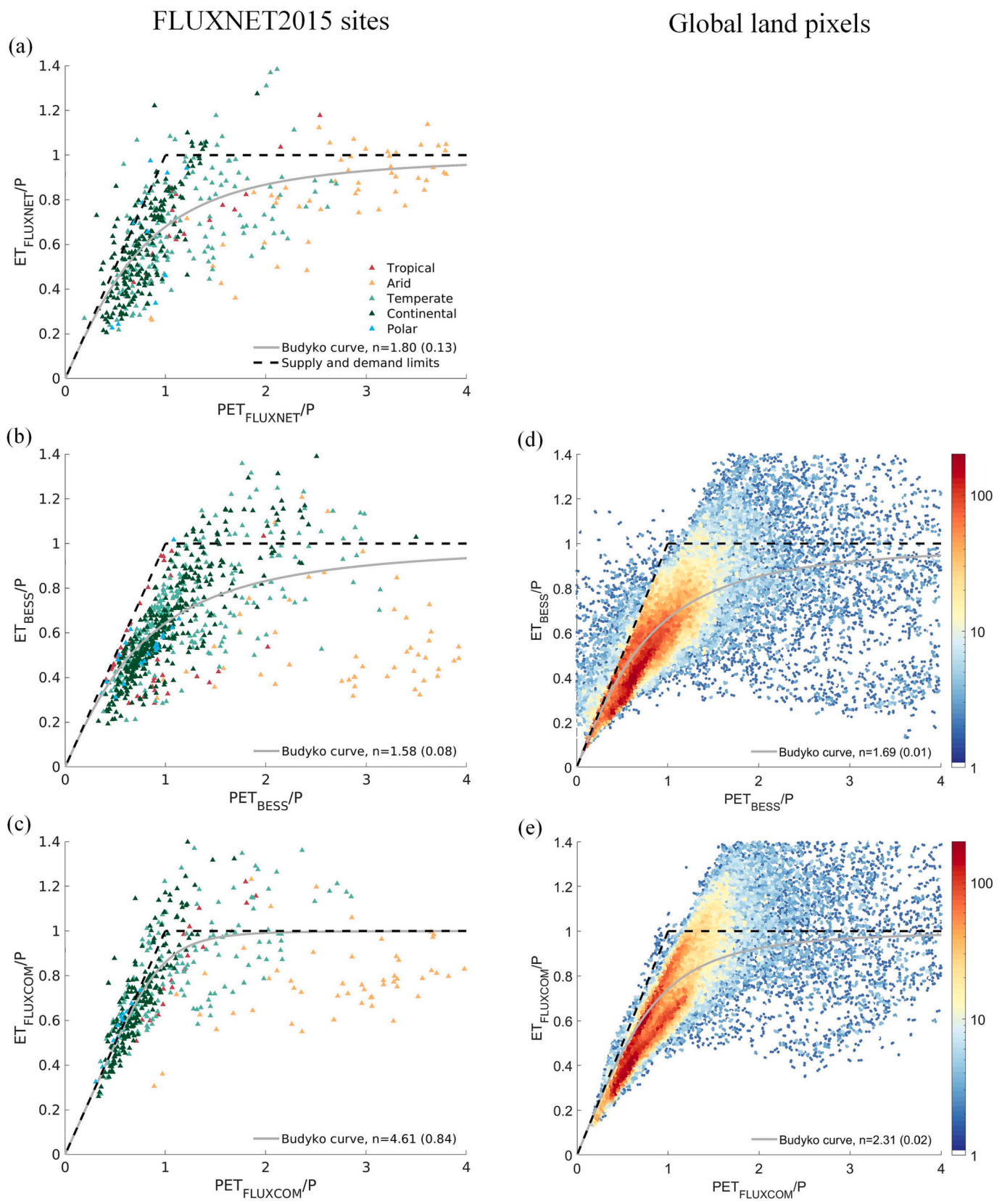

Fig. 6. Evaporative index (= ET/P) vs. dryness index (= PET/P) based on annual sums from EC observations (a), and BESS (b, d) and FLUXCOM (c, e) simulations. Demand and supply limits are indicated by dashed lines, and best-fit Budyko curves are indicated by solid lines. P data were derived from EC observations (left) and gap-filled Tropical Rainfall Measuring Mission (TRMM) data (right). (d, e) are density plots of the global estimates from BESS and FLUXCOM, respectively. Data in global estimates are mean annual sums for 2001–2014. Standard errors are given in brackets.

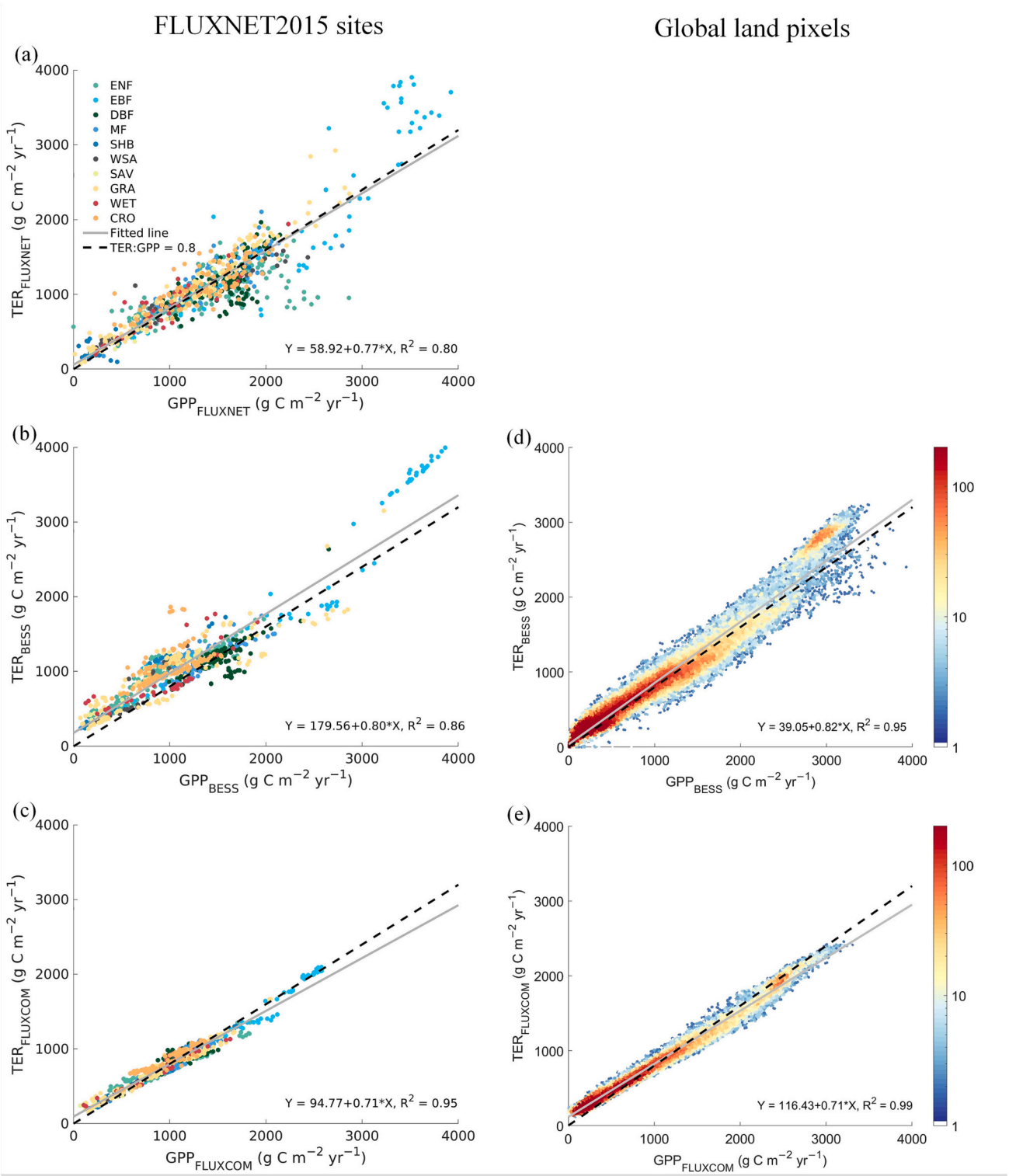

Fig. 7. Comparison of the relationship between annual sums of GPP and TER from various flux datasets over FLUXNET2015 sites (left) and all land pixels (right). (d, e) are density plots of the global estimates from BESS and FLUXCOM, respectively. Data in global estimates are mean annual sum values for 2001–2014.

4. Discussions

4.1. Are BESSv2.0 results consistent with other global datasets?

The coupled model, BESS, enabled us to quantify global annual budgets of radiation, energy, and carbon fluxes concurrently (Fig. 2). This is very important benefit by developing a coupled model as all flux variables were computed with the same forcing and each flux variable is constrained by the other flux variables, which were not available in the previous remote-sensing-based land surface flux products. Globally, SW at land surface was 861.30 ZJ yr^{-1}. PAR accounted for 46% of the SW energy (395.43 ZJ yr^{-1}), and only 39% of PAR was further absorbed by plants (i.e., fPAR = 0.39). Moreover, BESS quantified mean annual global total R_{net}, LE, GPP, TER, and NEE values (1982–2019) of 340.97

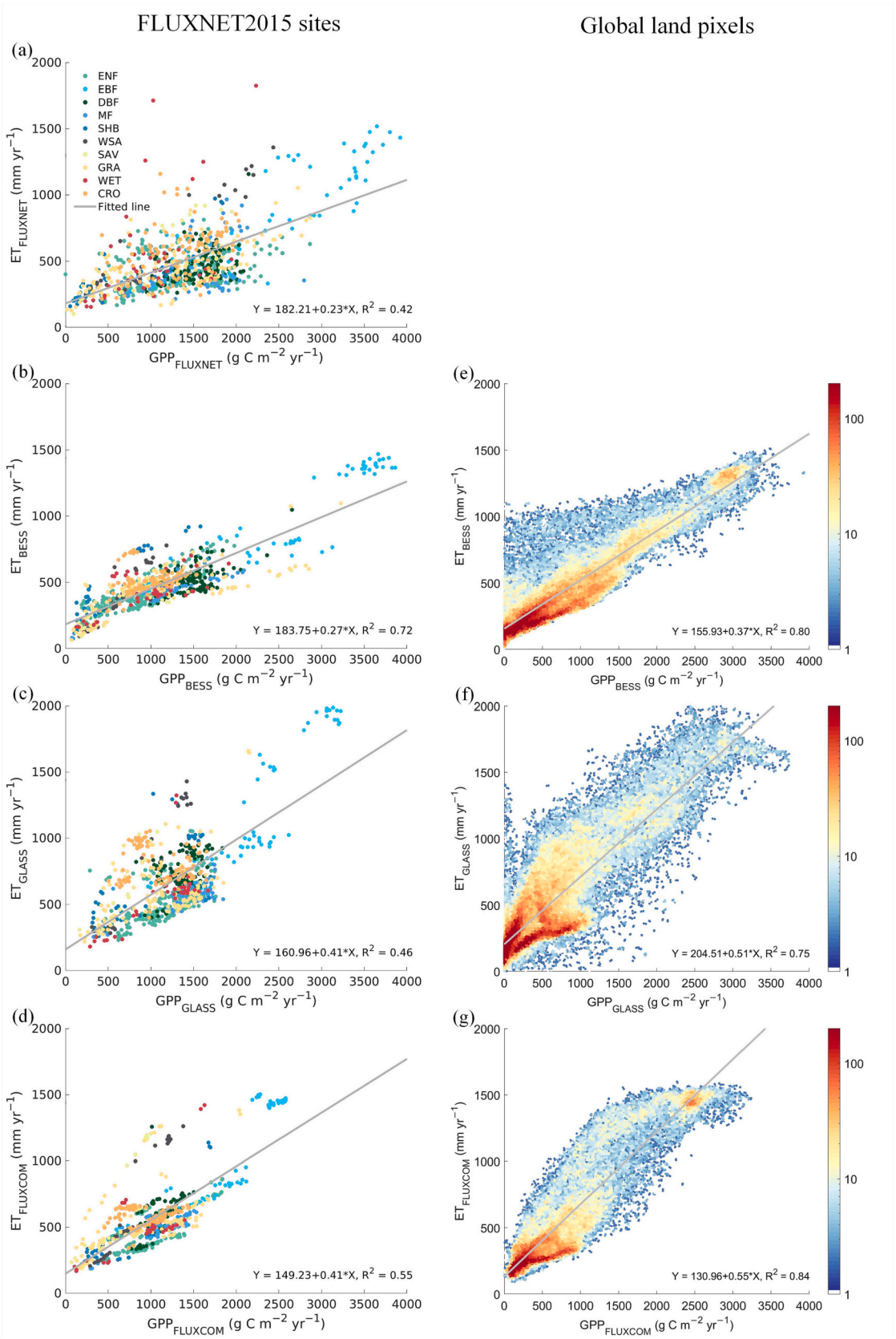

Fig. 8. Comparison of the relationships between annual sums of GPP and ET obtained from various flux datasets over FLUXNET2015 sites (left) and all land pixels (right). (e–g) are density plots of the global estimates from BESS, GLASS, and FLUXCOM, respectively. Data in global estimates are mean annual sums for 2001–2014.

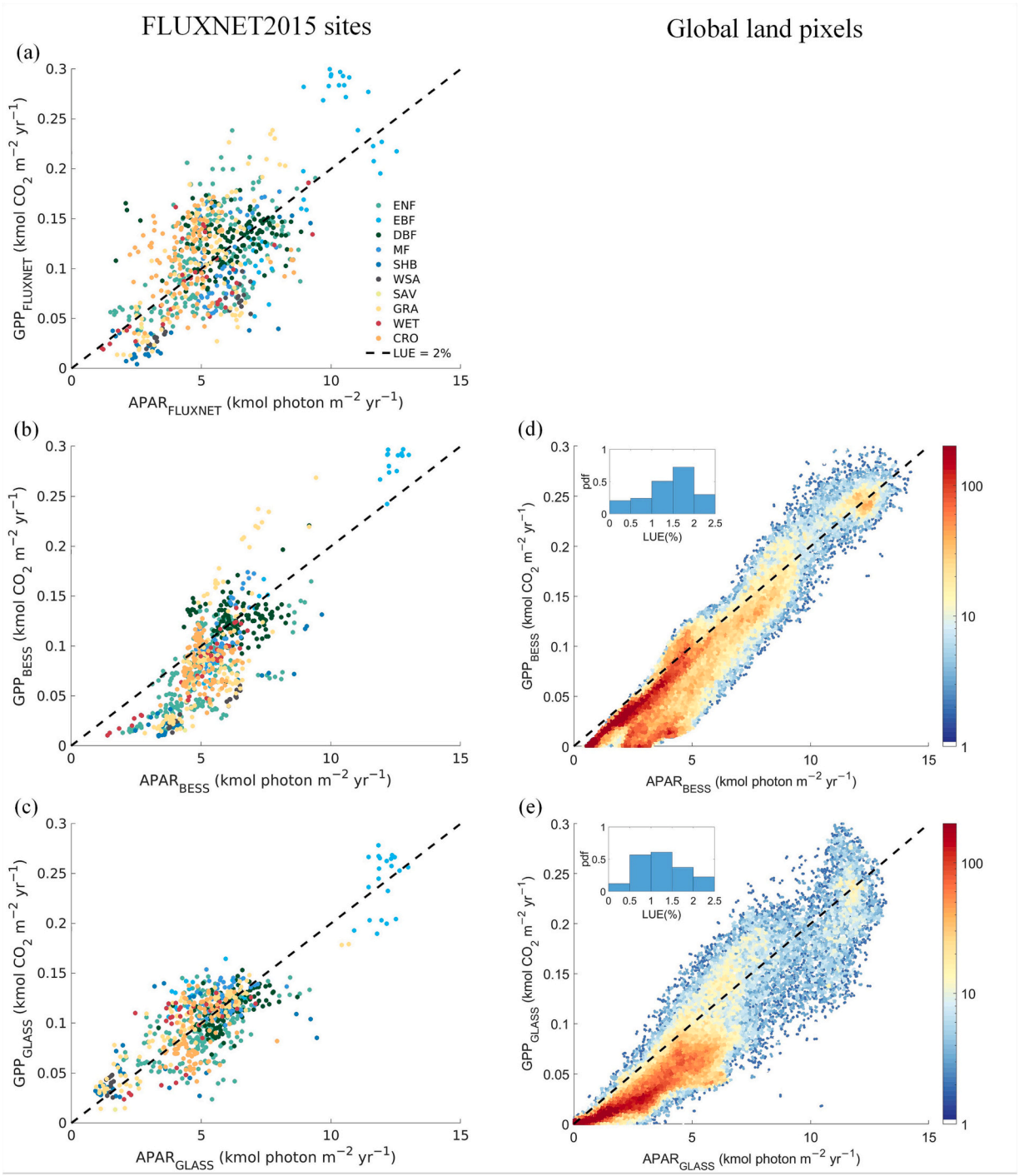

Fig. 9. Comparison of the relationships between annual sums of GPP and APAR obtained from various flux datasets over FLUXNET2015 sites (left) and all land pixels (right). (d, e) are density plots of the global estimates from BESS and GLASS, respectively. Data in global estimates are mean annual sums for 2001–2014. Dashed lines indicate 2% in LUE.

$\pm$ 5.22 ZJ yr^{-1} (mean $\pm$ 1 SD), 166.04 $\pm$ 1.78 ZJ yr^{-1}, 125.74 $\pm$ 5.95 Pg C yr^{-1}, 109.30 $\pm$ 3.16 Pg C yr^{-1}, and $-$ 16.28 $\pm$ 2.95 Pg C yr^{-1}, respectively (Fig. 2). Furthermore, BESS radiation and energy flux values were similar to the global estimates derived from the constrained CMIP5 products based on field observations (i.e., 859.46 $\pm$ 7.47 ZJ yr^{-1} for SW, 177.50 ZJ yr^{-1} for LE, 326.97 ZJ yr^{-1} for R_{net} (Wild et al., 2015)). Overall, BESS flux estimates were close to or within the range of other model estimates (Table S4).

Together, these BESS coupled fluxes enabled us to further corroborate the following ecosystem functional properties constrained by physical and ecological principles. First, globally, annual LUE was only 1.5%. Recent research has reported comparable LUE values derived from the ensemble of either DGVMs (1.33 $\pm$ 0.40%) or data-driven models (1.64 $\pm$ 0.46%) at global scale (Tang et al., 2020). This small number of LUE further decreased to 0.27% once we consider the fraction of global GPP to global land surface SW. Why only the tiny portion of solar energy is used for photosynthesis on annual timescales? Possible explanations may include that most solar energy occurs at wavelengths ineffective for photosynthesis (Kruse et al., 2005); photosynthesis is inactive for more than half of the year in many ecosystems due to

thermal limitation (Ganguly et al., 2010); ecosystems can hardly form closed canopies and absorb most of the incident light under nutrient and/or water limitations (Baldocchi and Penuelas, 2019).

Second, 87% of the assimilated carbon was respired back into the atmosphere (i.e., CUE = 0.87), which was consistent with data-driven estimates (Jung et al., 2011; Jung et al., 2020; Zeng et al., 2020) yet slightly higher than FLUXNET measurements on an annual basis (~0.82; Baldocchi and Penuelas, 2019; Fig. 7a). The bias might stem from a potential overestimation of TER in dry and cold regions (Fig. 5), where the FLUXNET sites were less represented in the model calibration process. By contrast, DGVMs and top-down estimates via atmospheric inversion models tended to yield even higher CUE (> 0.95; Table S4; Huang et al., 2016; Sitch et al., 2015). This discrepancy has been discussed with potential reasons such as non-respiratory CO_2 release (e.g., fire), riverine carbon export, and harvest in global ecosystems (Ballantyne et al., 2021; Zscheischler et al., 2017). Nevertheless, these results confirmed that TER consumes a significant portion of GPP (Baldocchi et al., 2001), and thus the magnitude of the global net carbon sink is minor compared to GPP. On the one hand, this is partly because supporting infrastructure (i.e., physical structures, such as roots, stems, and leaves, and processes that support carbon uptake) for carbon uptake requires significant respiratory costs (Waring et al., 1998); on the other hand, active photosynthetic period in many ecosystems is less than half of the year, whereas respiration may occur year-round.

Third, terrestrial ecosystems evaporated 67.67 × 10^3 km^3 of water while fixing 125.74 Pg C per year (i.e., WUE = 1.86 g C kg^{-1}-H_2O). This estimate is consistent with the individual DGVM WUE estimations (ranging from 1.81 to 2.09 g C kg^{-1}-H_2O) (Huang et al., 2015; Huang et al., 2016). Collectively, recent global evidence of convergence in WUE among many ecosystems (i.e., GRA, WET, SAV, DBF, and deciduous needleleaf forests) spanning diverse climates, with a similar average value of ~1.70 g C kg^{-1}-H_2O, reflects the trade-off that CO_2 uptake by vegetation is coupled to water loss by transpiration (Cooley et al., 2022; Xue et al., 2015).

4.2. BESSv2.0 performance

The BESS model exhibited comparable performance to other remote-sensing-driven benchmark models against FLUXNET observations across 206 sites (Fig. 3). There were no significant differences between evaluation results of BESS at 1-km and at 0.05° spatial resolutions (Table 2). The error metrics were comparable to those of FLUXCOM and GLASS, as well as estimates from the previous BESS version (R^2: 0.86 and 0.84 and NRMSE: 45% and 51% for ET and GPP, respectively, at 113 sites; see Jiang and Ryu (2016) for details). Although BESS accurately estimated coupled fluxes at daily and seasonal time scales overall, it performed less well on interannual predictions, especially for NEE. Similar findings showing lower model performance in explaining interannual flux variation have been reported in earlier studies that used either process-based (Jiang and Ryu, 2016; Keenan et al., 2012) or empirical models (Tramontana et al., 2016; Zeng et al., 2020). Given that process models typically calculate NEE as the difference between GPP and TER, the reduced NEE prediction accuracy was likely owing to the propagation of uncertainties from the two flux terms.

It was notable how estimates of energy and carbon fluxes showed strong differences in spatial patterns among models. In the tropics, BESS R_{net} was significantly (~30%) lower than FLUXCOM R_{net}, which partly explains the lower BESS ET within the same region. Similar to BESS, recent research showed an ensemble mean annual R_{net} of ~4100 MJ m^{-2} yr^{-1} for tropical forests, derived from four independent global R_{net} products (one remote-sensing product and three reanalysis products) (Jia et al., 2018). By contrast, FLUXCOM yielded ~20% and ~ 30% lower estimates than BESS for GPP and TER, respectively, resulting in FLUXCOM being a stronger carbon sink than BESS in the tropics (Fig. S2). The weaker tropical carbon sink obtained by BESS appeared to be consistent with the findings of recent observational studies (Gatti et al., 2021; Hubau et al., 2020; Restrepo-Coupe et al., 2017). GLASS showed larger ET values than BESS over most EBF regions (Fig. S3). There are several possible sources for these inconsistencies. First, the reliability of remote-sensing products usually fall prey to low quality of forcing data in the tropics caused by the long-duration cloud contamination. Second, the seasonal pattern of land–atmosphere fluxes (in particular, carbon fluxes) may not closely follow that of the vegetation indices but be more sensitive to the meteorological factors (e.g., T_a) (Tramontana et al., 2016). Third, less prominent seasonal variation obtained by satellite-derived key forcing data (e.g., vegetation indices) and insufficient spatial coverage of tropical forest sites likely contributed to the comparably low performance in data-driven modeling (Yao et al., 2014). Due to the absence of calibration process (except for TER), BESS fluxes were not expected to be influenced by non-representative sampling data. Notwithstanding the above findings, it remains challenging to determine the accuracy of divergent tropical flux estimations based on limited EC measurement data. At least 50% of crop regions were characterized by both BESS ~ FLUXCOM and BESS ~ GLASS GPP deviations >500 g C m^{-2} yr^{-1}. The limitations of CRO GPP patterns could be attributed to two main factors: (1) incomplete capturing of environmental stresses or agricultural management activities by coarse-resolution forcing data; and (2) low quality of remote-sensing forcing data over CRO. For example, as a key input variable of all three models, several studies have reported either MODIS or GLASS LAI was generally underestimated in CRO (Claverie et al., 2013; Fang et al., 2019), potentially lowering the corresponding annual GPP estimates. This was also reflected in site-level GPP evaluations that all three products consistently showed underestimation over CRO sites (Table S5). Additionally, FLUXCOM showed the largest negative bias over CRO, partly due to the absence of distinguishing between C3 and C4 crops in the machine-learning algorithms (Tramontana et al., 2016).

In this study, we observed large uncertainties in global terrestrial energy and carbon budget estimates. The range of the magnitudes in annual flux budgets among various global products remained to be wide (Table S4), despite substantial advances in observation, modeling, and satellite remote sensing of land–atmosphere fluxes. Both theory and evidence have pointed to CO_2 fertilization as a primary cause of enhanced global carbon uptake (Chen et al., 2022); however, most remote-sensing-based models have not explicitly incorporated CO_2 fertilization effects (Chen et al., 2012; Tagesson et al., 2021; Zhang et al., 2016; Zhang et al., 2017). Only FLUXCOM demonstrated no discernible trend in carbon flux products, probably due to the absence of CO_2 fertilization in the model algorithms (Jung et al., 2020). BESS NEE showed a downward trend (increased carbon sink) which is the opposite to both GPP and TER trends. It appeared as GPP trend was stronger than TER trend. There was a stronger oscillation, with lower magnitudes, in BESS global R_{net} values before 2000, in contrast to the period after 2001. MODIS-derived BESS SW, PAR and diffuse PAR were evaluated comprehensively, which agreed at tower, regional to global scales from snapshot to annual sum estimates (Ryu et al., 2018). However, during pre-MODIS era, BESS SW relied on ERA5 that was calibrated with BESS SW during MODIS period, and we found the ERA5 SW in pre-MODIS era showed larger year-to-year variations and lower estimates than MODIS era (Fig. 4). As SW forms the key components in R_{net}, we assume that ERA5 SW data partly explains the lower values in BESS R_{net} during pre-MODIS period than MODIS period. Moreover, albedo also plays an important role in BESS R_{net} estimation (Jiang and Ryu, 2016). We observed a decline circa 2000–2001 in time series of visible, NIR, and SW albedo datasets, which is likely to increase R_{net} value accordingly (Fig. S4).

4.3. Implications of functional evaluations

The derived ecosystem functional properties provided deeper insight into the sources of uncertainty in global land–atmosphere flux simulations. First, BESS ET was well-constrained by the two fundamental upper

bounds in Budyko space. The curvature parameters in the Budyko relation obtained from both BESS and FLUXNET data were consistent with those derived from the global syntheses (Choudhury, 1999; Pike, 1964). Nevertheless, a few data above the demand and supply limits may indicate contributions from water sources other than precipitation (i.e. groundwater), or the influence of site-specific climate types, which is a major determinant of the evaporative index (ET/P) (Fig. 6) (Williams et al., 2012). Furthermore, the overall lower evaporative index obtained by BESS in arid regions (Fig. 6b) compared to FLUXNET measurements indicated overestimated losses to runoff or deep drainage (Greve et al., 2016). Theoretically, the evaporative index in dry regions must approach 1 as most precipitation will return to the atmosphere via ET. In Ball-Berry model, we applied a water stress factor to the Ball-Berry intercept (Eq. 8–10). It was necessary to constrain seasonal patterns of ET in dry regions (Fig. S5), but the low evaporative index in dry sites within the Budyko framework suggest our water stress factor overcorrected water stress effects on annual sum scale. It indicates that BESSv2.0 misses some mechanism about water stress effects that link seasonal to annual scales, which will be our future study. For FLUXCOM (Fig. 6c, e), it was evident that substantial data appeared that exceeded 1 in evaporative index in both flux tower pixels and global pixels, indicating annual ET exceeded annual precipitation. On the other hand, FLUXCOM evaporative index in dry sites approached to 1 (Fig. 6c), which is consistent with FLUXNET datasets (Fig. 6a). Overall, the Budyko relation revealed the missing mechanisms in BESS and FLUXCOM.

Second, BESS produced an overall CUE of approximately 0.8, as well as a significant positive correlation between annual GPP and TER at both the site and global scales. These results corroborated evidence from the FLUXNET observations (Fig. 7), as well as the findings of many previous studies (Baldocchi, 2020). However, FLUXCOM displayed a lower CUE than BESS at both the site and global scales, largely driven by differences over Arctic and tropical regions (Fig. S2). Furthermore, a very strong linear relationship ($R^2 \geq 0.95$) between FLUXCOM TER and GPP is likely unrealistic, due to the small variation in CUE across PFTs associated with environmental stresses, in contrast to both FLUXNET and BESS data. FLUXCOM (RS setup) estimations relied exclusively on remote-sensing-based land-surface properties (e.g., vegetation indices and land-surface temperatures), which insufficiently captured environmental stress effects on carbon fluxes without additional meteorological forcing (e.g., T_a and VPD). According to published eddy covariance observations, CUE can either be <0.6 in ENF and DBF sites (without stresses), or approach 1 in mature EBF sites (Baldocchi and Penuelas, 2019; Luyssaert et al., 2007), whereas TER can exceed GPP over herbaceous (e.g., grasslands) or disturbed sites (Baldocchi, 2008). Overall, BESS CUE was consistent with those published datasets. Globally, BESS annual CUE displayed a slightly negative trend (-0.001 yr^{-2}), indicating a growing land carbon sink over recent decades (Fig. 4). Such trend was more apparent in annual NEE estimates, which was largely triggered by that CO_2 fertilization enhanced GPP more than TER, alongside the effects of land cover and climate change, forest regrowth (Fernández-Martínez et al., 2019; Fernández-Martínez et al., 2017).

Third, BESS WUE was more consistent to FLUXNET while GLASS and FLUXCOM presented lower WUE values than FLUXNET. In particular, a large portion of GLASS (58.1% for DBF and 56.6% for CRO) and FLUXCOM (57.4% for DBF and 38.7% for CRO) WUE estimates over DBF and CRO sites was <2.0 and < 1.5 g C kg^{-1}-H_2O, respectively (Fig. S6). These outcomes were lower than those observed in previous studies that suggested at least ~2.7 and ~ 1.8 g C kg^{-1}-H_2O of WUE for DBF and CRO sites, respectively (Law et al., 2002; Tang et al., 2014). Moreover, consistent with a recent study (Knauer et al., 2017), BESS captured a ~ 0.01 g C kg^{-1}-H_2O increase per year in WUE worldwide over the past four decades (Fig. 4). This finding supports the assumption that WUE would be enhanced in elevated CO_2 environments because of partial stomatal closure and conservative maintenance of the internal-to-atmospheric CO_2 concentration ratio (Keenan et al., 2013; Wong et al., 1979). In addition, the convergence of fitted intercepts in linear regression analysis across different datasets indicated that, for ecosystem photosynthesis to exceed zero, rainfall must exceed ~150 mm yr^{-1} to compensate water evaporation from soil by assuming negligible contributions from other water sources (Fig. 8).

Finally, BESS LUE on annual scales was well constrained by 2% while it revealed discrepancy at PFT levels compared to FLUXNET. Previous studies reported that annual LUE at flux towers were at most 2% and were downregulated by environmental stresses (Baldocchi and Penuelas, 2019; Ryu et al., 2019). BESS annual LUE also revealed that upper limit was around 2% (Fig. 9b, d). When investigating at individual PFT level (Fig. S7), several lessons were found. First, BESS showed highest LUE in EBF where clouds pervade so diffuse light is dominant. Higher diffuse fraction leads more photons to penetrate canopies deeper, which can enhance photosynthesis in shaded leaves that are light-limited (Alton et al., 2007; Knohl and Baldocchi, 2008). Therefore, LUE tends to increase with higher diffuse fraction. Second, LUE showed large variations in each PFT (Figs. 9 and S4), supporting the conclusion that the PFT categories were generally not good indicators of spatial LUE variability (He et al., 2022; Schwalm et al., 2006). Third, FLUXNET showed highest LUE in CRO where BESS LUE was around half of FLUXNET. As we used MODIS fPAR to compute APAR in FLUXNET LUE, we assume that the tendency of underestimated MODIS fPAR in crop regions might lead higher LUE in FLUXNET data (Wang et al., 2017b; Zhang et al., 2008). We believe that scale match between flux tower footprints and satellite pixel is very important in crop landscapes which often include C3 and C4 rotation in space and time and include other land covers. Using higher spatial resolution satellite data such as CubeSats could help to estimate LUE precisely in crop sites (Kong et al., 2022; Li et al., 2008). The static, coarse-resolution C3/C4 fraction map used in BESS could be another source of uncertainty. On top of these, more datasets and studies are required to examine if the reported long-term trend of global LUE by BESS is robust.

5. Conclusions

In this study, we generated a set of global daily R_{net}, ET, GPP, TER, and NEE products at 0.05° resolution from 1982 to 2019, using BESS (v2.0), a remote-sensing-based, coupled process model. These products were comprehensively assessed via both direct and functional evaluations against FLUXNET observations across temporal scales, as well as comparisons against the benchmark products at site and global scales. BESS provided individual flux products with accuracy comparable to the benchmark global products; more importantly, BESS performed much better in retrieving functional properties such as the Budyko relation, CUE, WUE, and LUE, showing upward trends in global WUE (0.009 g C kg^{-1}-H_2O yr^{-2}) and LUE (0.005% yr^{-2}), but a downward trend in global CUE (-0.001 yr^{-2}). BESS showed the advantages of a fully coupled model structure, and the robust model performance in concurrently investigating ecosystem functional properties at the global scale, which was not the case for most other remote-sensing-driven models. Overall, BESS produces a set of reliable and independent products from other global data-driven products, and is expected to facilitate studies diagnosing the state of terrestrial ecosystems in a coupled and comprehensive manner. BESS flux products are publicly available at https://www.environment.snu.ac.kr/data/ and will be updated periodically.

CRediT authorship contribution statement

Bolun Li: Conceptualization, Data curation, Formal analysis, Investigation, Validation, Visualization, Writing – original draft. **Youngryel Ryu:** Conceptualization, Funding acquisition, Project administration, Resources, Supervision, Writing – review & editing. **Chongya Jiang:** Conceptualization, Investigation, Validation, Writing – review & editing. **Benjamin Dechant:** Conceptualization, Investigation, Writing – review & editing. **Jiangong Liu:** Conceptualization, Investigation,

Writing – review & editing. **Yulin Yan:** Conceptualization, Investigation, Writing – review & editing. **Xing Li:** Conceptualization, Investigation, Writing – review & editing.

Declaration of Competing Interest

None.

Data availability

The data will be freely available

Acknowledgements

This study was funded by National Research Foundation of Korea (NRF-2019R1A2C2084626, NRF-2021M1A5A1065681). YR, JL, XL were supported by the LEMONTREE (Land Ecosystem Models based On New Theory, obseRvations and ExperimEnts) project, funded through the generosity of Eric and Wendy Schmidt by recommendation of the Schmidt Futures program. B.D. was supported by sDiv, the Synthesis Centre of iDiv (DFG FZT 118, 202548816). We thank all people who provided datasets used in this study, in particular, the TRENDY team for sharing the DGVM simulations (https://blogs.exeter.ac.uk/trendy/), Dr. Martin Jung and Ulrich Weber for sharing the FLUXCOM products, and Prof. Trevor Keenan (trevorkeenan@lbl.gov) for sharing PR model outputs.

Appendix A. Supplementary data

Supplementary data to this article can be found online at https://doi.org/10.1016/j.rse.2023.113696.

References

Alton, P.B., North, P.R., Los, S.O., 2007. The impact of diffuse sunlight on canopy light-use efficiency, gross photosynthetic product and net ecosystem exchange in three forest biomes. Glob. Chang. Biol. 13, 776–787.
Bae, J., Ryu, Y., 2017. Spatial and temporal variations in soil respiration among different land cover types under wet and dry years in an urban park. Landsc. Urban Plan. 167, 378–385.
Baldocchi, D., 2008. Breathing of the terrestrial biosphere: lessons learned from a global network of carbon dioxide flux measurement systems. Aust. J. Bot. 56, 1–26.
Baldocchi, D., 2020. How Eddy covariance flux measurements have contributed to our understanding of global change biology. Glob. Chang. Biol. 26, 242–260.
Baldocchi, D., Chu, H., Reichstein, M., 2018. Inter-annual variability of net and gross ecosystem carbon fluxes: a review. Agric. For. Meteorol. 249, 520–533.
Baldocchi, D., Falge, E., Gu, L., Olson, R., Hollinger, D., Running, S., Anthoni, P., Bernhofer, C., Davis, K., Evans, R., 2001. FLUXNET: a new tool to study the temporal and spatial variability of ecosystem-scale carbon dioxide, water vapor, and energy flux densities. Bull. Am. Meteorol. Soc. 82, 2415–2434.
Baldocchi, D., Meyers, T., 1998. On using eco-physiological, micrometeorological and biogeochemical theory to evaluate carbon dioxide, water vapor and trace gas fluxes over vegetation: a perspective. Agric. For. Meteorol. 90, 1–25.
Baldocchi, D., Penuelas, J., 2019. The physics and ecology of mining carbon dioxide from the atmosphere by ecosystems. Glob. Chang. Biol. 25, 1191–1197.
Baldocchi, D., Ryu, Y., Keenan, T., 2016. Terrestrial Carbon Cycle Variability [version 1; peer review: 2 approved]. F1000Research 5.
Ball, J.T., 1988. An analysis of stomatal conductance. In: Stanford University Stanford.
Ballantyne, A.P., Liu, Z., Anderegg, W.R., Yu, Z., Stoy, P., Poulter, B., Vanderwall, J., Watts, J., Kelsey, K., Neff, J., 2021. Reconciling carbon-cycle processes from ecosystem to global scales. Front. Ecol. Environ. 19, 57–65.
Bastos, A., Ciais, P., Friedlingstein, P., Sitch, S., Pongratz, J., Fan, L., Wigneron, J.P., Weber, U., Reichstein, M., Fu, Z., Anthoni, P., Arneth, A., Haverd, V., Jain, A.K., Joetzjer, E., Knauer, J., Lienert, S., Loughran, T., McGuire, P.C., Tian, H., Viovy, N., Zaehle, S., 2020. Direct and seasonal legacy effects of the 2018 heat wave and drought on European ecosystem productivity. Sci. Adv. 6, eaba2724.
Batjes, N.H., Ribeiro, E., van Oostrum, A., 2020. Standardised soil profile data to support global mapping and modelling (WoSIS snapshot 2019). Earth Syst. Sci. Data 12, 299–320.
Bernacchi, C.J., Singsaas, E.L., Pimentel, C., Portis Jr., A.R., Long, S.P., 2001. Improved temperature response functions for models of rubisco-limited photosynthesis. Plant Cell Environ. 24, 253–259.
Bisht, G., Venturini, V., Islam, S., Jiang, L., 2005. Estimation of the net radiation using MODIS (Moderate resolution imaging Spectroradiometer) data for clear sky days. Remote Sens. Environ. 97, 52–67.
Budyko, M.I., 1974. Climate and Life. Academic Press.
Chapin, F.S., Woodwell, G.M., Randerson, J.T., Rastetter, E.B., Lovett, G.M., Baldocchi, D.D., Clark, D.A., Harmon, M.E., Schimel, D.S., Valentini, R., Wirth, C., Aber, J.D., Cole, J.J., Goulden, M.L., Harden, J.W., Heimann, M., Howarth, R.W., Matson, P.A., McGuire, A.D., Melillo, J.M., Mooney, H.A., Neff, J.C., Houghton, R.A., Pace, M.L., Ryan, M.G., Running, S.W., Sala, O.E., Schlesinger, W.H., Schulze, E.D., 2006. Reconciling carbon-cycle concepts, terminology, and methods. Ecosystems 9, 1041–1050.
Chen, C., Riley, W.J., Prentice, I.C., Keenan, T.F., 2022. CO2 fertilization of terrestrial photosynthesis inferred from site to global scales. Proc. Natl. Acad. Sci. 119, e2115627119.
Chen, J.M., Liu, J., Cihlar, J., Goulden, M.L., 1999. Daily canopy photosynthesis model through temporal and spatial scaling for remote sensing applications. Ecol. Model. 124, 99–119.
Chen, J.M., Mo, G., Pisek, J., Liu, J., Deng, F., Ishizawa, M., Chan, D., 2012. Effects of foliage clumping on the estimation of global terrestrial gross primary productivity. Global Biogeochem. Cycles 26.
Chen, S., Huang, Y., Zou, J., Shen, Q., Hu, Z., Qin, Y., Chen, H., Pan, G., 2010. Modeling interannual variability of global soil respiration from climate and soil properties. Agric. For. Meteorol. 150, 590–605.
Choudhury, B., 1999. Evaluation of an empirical equation for annual evaporation using field observations and results from a biophysical model. J. Hydrol. 216, 99–110.
Chu, H., Baldocchi, D.D., John, R., Wolf, S., Reichstein, M., 2017. Fluxes all of the time? A primer on the temporal representativeness of FLUXNET. J.Geophys.Res.Biogeosci. 122, 289–307.
Claverie, M., Vermote, E.F., Weiss, M., Baret, F., Hagolle, O., Demarez, V., 2013. Validation of coarse spatial resolution LAI and FAPAR time series over cropland in Southwest France. Remote Sens. Environ. 139, 216–230.
Collatz, G., Ribas-Carbo, M., Berry, J., 1992. Coupled photosynthesis-stomatal conductance model for leaves of C4 plants. Funct. Plant Biol. 19, 519–538.
Cooley, S.S., Fisher, J.B., Goldsmith, G.R., 2022. Convergence in water use efficiency within plant functional types across contrasting climates. Nat.Plants 8, 341–345.
Dai, Y., Shangguan, W., Wei, N., Xin, Q., Yuan, H., Zhang, S., Liu, S., Lu, X., Wang, D., Yan, F., 2019. A review of the global soil property maps for earth system models. Soil 5, 137–158.
De Pury, D.G.G., Farquhar, G.D., 1997. Simple scaling of photosynthesis from leaves to canopies without the errors of big-leaf models. Plant Cell Environ. 20, 537–557.
Defourny, P., Kirches, G., Brockmann, C., Boettcher, M., Peters, M., Bontemps, S., Lamarche, C., Schlerf, M., Santoro, M., 2012. Land cover CCI. Product User Guide Version, 2, 325.
Dimiceli, C., Carroll, M., Sohlberg, R., Kim, D., Kelly, M., Townshend, J., 2015. MOD44B MODIS/terra vegetation continuous fields yearly L3 global 250m SIN grid V006. NASA EOSDIS Land Processes DAAC.
Fang, H., Zhang, Y., Wei, S., Li, W., Ye, Y., Sun, T., Liu, W., 2019. Validation of global moderate resolution leaf area index (LAI) products over croplands in northeastern China. Remote Sens. Environ. 233, 111377.
Farquhar, G.D., von Caemmerer, S., Berry, J.A., 1980. A biochemical model of photosynthetic CO2 assimilation in leaves of C3 species. Planta 149, 78–90.
Feng, J., Wang, J., Song, Y., Zhu, B., 2018. Patterns of soil respiration and its temperature sensitivity in grassland ecosystems across China. Biogeosciences 15, 5329–5341.
Fernández-Martínez, M., Sardans, J., Chevallier, F., Ciais, P., Obersteiner, M., Vicca, S., Canadell, J.G., Bastos, A., Friedlingstein, P., Sitch, S., Piao, S.L., Janssens, I.A., Peñuelas, J., 2019. Global trends in carbon sinks and their relationships with CO2 and temperature. Nat. Clim. Chang. 9, 73–79.
Fernández-Martínez, M., Vicca, S., Janssens, I.A., Ciais, P., Obersteiner, M., Bartrons, M., Sardans, J., Verger, A., Canadell, J.G., Chevallier, F., Wang, X., Bernhofer, C., Curtis, P.S., Gianelle, D., Grünwald, T., Heinesch, B., Ibrom, A., Knohl, A., Laurila, T., Law, B.E., Limousin, J.M., Longdoz, B., Loustau, D., Mammarella, I., Matteucci, G., Monson, R.K., Montagnani, L., Moors, E.J., Munger, J.W., Papale, D., Piao, S.L., Peñuelas, J., 2017. Atmospheric deposition, CO2, and change in the land carbon sink. Sci. Rep. 7, 9632.
Fisher, J.B., Tu, K.P., Baldocchi, D.D., 2008. Global estimates of the land–atmosphere water flux based on monthly AVHRR and ISLSCP-II data, validated at 16 FLUXNET sites. Remote Sens. Environ. 112, 901–919.
Friedl, M., Sulla-Menashe, D., 2015. MCD12C1 MODIS/Terra+ Aqua Land Cover Type Yearly L3 Global 0.05 Deg CMG V006, NASA EOSDIS Land Processes DAAC. https://doi.org/10.5067/MODIS/MCD12C1. 006.
Ganguly, S., Friedl, M.A., Tan, B., Zhang, X., Verma, M., 2010. Land surface phenology from MODIS: characterization of the collection 5 global land cover dynamics product. Remote Sens. Environ. 114, 1805–1816.
Gatti, L.V., Basso, L.S., Miller, J.B., Gloor, M., Gatti Domingues, L., Cassol, H.L.G., Tejada, G., Aragão, L.E.O.C., Nobre, C., Peters, W., Marani, L., Arai, E., Sanches, A. H., Corrêa, S.M., Anderson, L., Von Randow, C., Correia, C.S.C., Crispim, S.P., Neves, R.A.L., 2021. Amazonia as a carbon source linked to deforestation and climate change. Nature 595, 388–393.
Gentine, P., Green, J.K., Guérin, M., Humphrey, V., Seneviratne, S.I., Zhang, Y., Zhou, S., 2019. Coupling between the terrestrial carbon and water cycles—a review. Environ. Res. Lett. 14, 083003.
Greve, P., Gudmundsson, L., Orlowsky, B., Seneviratne, S.I., 2016. A two-parameter budyko function to represent conditions under which evapotranspiration exceeds precipitation. Hydrol. Earth Syst. Sci. 20, 2195–2205.
Haario, H., Laine, M., Mira, A., Saksman, E., 2006. DRAM: Efficient adaptive MCMC. StCom 16, 339–354.
Haario, H., Saksman, E., Tamminen, J., 2001. An adaptive metropolis algorithm. Bern 7, 223–242.
Hansen, M., Song, X., 2018. Vegetation continuous fields (VCF) yearly global 0.05 deg. NASA EOSDIS land processes DAAC.

He, M., Chen, S., Lian, X., Wang, X., Peñuelas, J., Piao, S., 2022. Global spectrum of vegetation light-use efficiency. Geophys. Res. Lett. 49 e2022GL099550.
Hengl, T., Mendes de Jesus, J., Heuvelink, G.B.M., Ruiperez Gonzalez, M., Kilibarda, M., Blagotić, A., Shangguan, W., Wright, M.N., Geng, X., Bauer-Marschallinger, B., Guevara, M.A., Vargas, R., MacMillan, R.A., Batjes, N.H., Leenaars, J.G.B., Ribeiro, E., Wheeler, I., Mantel, S., Kempen, B., 2017. SoilGrids250m: global gridded soil information based on machine learning. PLOS ONE 12, e0169748.
Hersbach, H., Bell, B., Berrisford, P., Biavati, G., Horányi, A., Muñoz Sabater, J., Nicolas, J., Peubey, C., Radu, R., Rozum, I., 2018. ERA5 hourly data on single levels from 1979 to present. Copernicus Climate Change Service (C3S) Climate Data Store (CDS), 10.
Huang, M., Piao, S., Sun, Y., Ciais, P., Cheng, L., Mao, J., Poulter, B., Shi, X., Zeng, Z., Wang, Y., 2015. Change in terrestrial ecosystem water-use efficiency over the last three decades. Glob. Chang. Biol. 21, 2366–2378.
Huang, S., Bartlett, P., Arain, M.A., 2016. An analysis of global terrestrial carbon, water and energy dynamics using the carbon–nitrogen coupled CLASS-CTEMN+ model. Ecol. Model. 336, 36–56.
Huang, Y., Ryu, Y., Jiang, C., Kimm, H., Kim, S., Kang, M., Shim, K., 2018. BESS-Rice: a remote sensing derived and biophysical process-based rice productivity simulation model. Agric. For. Meteorol. 256–257, 253–269.
Hubau, W., Lewis, S.L., Phillips, O.L., Affum-Baffoe, K., Beeckman, H., Cuní-Sanchez, A., Daniels, A.K., Ewango, C.E.N., Fauset, S., Mukinzi, J.M., Sheil, D., Sonké, B., Sullivan, M.J.P., Sunderland, T.C.H., Taedoumg, H., Thomas, S.C., White, L.J.T., Abernethy, K.A., Adu-Bredu, S., Amani, C.A., Baker, T.R., Banin, L.F., Baya, F., Begne, S.K., Bennett, A.C., Benedet, F., Bitariho, R., Bocko, Y.E., Boeckx, P., Boundja, P., Brienen, R.J.W., Brncic, T., Chezeaux, E., Chuyong, G.B., Clark, C.J., Collins, M., Comiskey, J.A., Coomes, D.A., Dargie, G.C., de Haulleville, T., Kamdem, M.N.D., Doucet, J.-L., Esquivel-Muelbert, A., Feldpausch, T.R., Fofanah, A., Foli, E.G., Gilpin, M., Gloor, E., Gonmadje, C., Gourlet-Fleury, S., Hall, J.S., Hamilton, A.C., Harris, D.J., Hart, T.B., Hockemba, M.B.N., Hladik, A., Ifo, S.A., Jeffery, K.J., Jucker, T., Yakusu, E.K., Kearsley, E., Kenfack, D., Koch, A., Leal, M.E., Levesley, A., Lindsell, J.A., Lisingo, J., Lopez-Gonzalez, G., Lovett, J.C., Makana, J.-R., Malhi, Y., Marshall, A.R., Martin, J., Martin, E.H., Mbayu, F.M., Medjibe, V.P., Mihindou, V., Mitchard, E.T.A., Moore, S., Munishi, P.K.T., Bengone, N.N., Ojo, L., Ondo, F.E., Peh, K.S.H., Pickavance, G.C., Poulsen, A.D., Poulsen, J.R., Qie, L., Reitsma, J., Rovero, F., Swaine, M.D., Talbot, J., Taplin, J., Taylor, D.M., Thomas, D.W., Toirambe, B., Mukendi, J.T., Tuagben, D., Umunay, P. M., van der Heijden, G.M.F., Verbeeck, H., Vleminckx, J., Willcock, S., Wöll, H., Woods, J.T., Zemagho, L., 2020. Asynchronous carbon sink saturation in african and amazonian tropical forests. Nature 579, 80–87.
Huffman, G.J., Bolvin, D.T., Nelkin, E.J., Wolff, D.B., Adler, R.F., Gu, G., Hong, Y., Bowman, K.P., Stocker, E.F., 2007. The TRMM multisatellite precipitation analysis (TMPA): quasi-global, multiyear, combined-sensor precipitation estimates at fine scales. J. Hydrometeorol. 8, 38–55.
IARC Working Group on the Evaluation of Carcinogenic Risks to Humans. Radiation. Lyon (FR): International Agency for Research on Cancer; 2012. (IARC Monographs on the Evaluation of Carcinogenic Risks to Humans, No. 100D.) SOLAR AND ULTRAVIOLET RADIATION. Available from: https://www.ncbi.nlm.nih.gov/books/NBK304366/.
Janssens, I.A., Lankreijer, H., Matteucci, G., Kowalski, A.S., Buchmann, N., Epron, D., Pilegaard, K., Kutsch, W., Longdoz, B., Grünwald, T., Montagnani, L., Dore, S., Rebmann, C., Moors, E.J., Grelle, A., Rannik, Ü., Morgenstern, K., Oltchev, S., Clement, R., Guðmundsson, J., Minerbi, S., Berbigier, P., Ibrom, A., Moncrieff, J., Aubinet, M., Bernhofer, C., Jensen, N.O., Vesala, T., Granier, A., Schulze, E.-D., Lindroth, A., Dolman, A.J., Jarvis, P.G., Ceulemans, R., Valentini, R., 2001. Productivity overshadows temperature in determining soil and ecosystem respiration across European forests. Glob. Chang. Biol. 7, 269–278.
Jarvis, A., Reuter, H.I., Nelson, A., Guevara, E., 2008. In: Hole-filled SRTM for the globe Version 4. available from the CGIAR-CSI SRTM 90m Database, 15, p. 5. http://srtm.csi.cgiar.org.
Jia, A., Liang, S., Jiang, B., Zhang, X., Wang, G., 2018. Comprehensive assessment of global surface net radiation products and uncertainty analysis. J.Geophys.Res. Atmos. 123, 1970–1989.
Jian, J., Bahn, M., Wang, C., Bailey, V.L., Bond-Lamberty, B., 2020. Prediction of annual soil respiration from its flux at mean annual temperature. Agric. For. Meteorol. 287, 107961.
Jiang, C., Ryu, Y., 2016. Multi-scale evaluation of global gross primary productivity and evapotranspiration products derived from breathing earth system simulator (BESS). Remote Sens. Environ. 186, 528–547.
Jiang, C., Ryu, Y., Wang, H., Keenan, T.F., 2020. An optimality-based model explains seasonal variation in C3 plant photosynthetic capacity. Glob. Chang. Biol. 26, 6493–6510.
Jung, M., Reichstein, M., Margolis, H.A., Cescatti, A., Richardson, A.D., Arain, M.A., Arneth, A., Bernhofer, C., Bonal, D., Chen, J., Gianelle, D., Gobron, N., Kiely, G., Kutsch, W., Lasslop, G., Law, B.E., Lindroth, A., Merbold, L., Montagnani, L., Moors, E.J., Papale, D., Sottocornola, M., Vaccari, F., Williams, C., 2011. Global patterns of land-atmosphere fluxes of carbon dioxide, latent heat, and sensible heat derived from eddy covariance, satellite, and meteorological observations. J. Geophys. Res. Biogeosci. 116.
Jung, M., Schwalm, C., Migliavacca, M., Walther, S., Camps-Valls, G., Koirala, S., Anthoni, P., Besnard, S., Bodesheim, P., Carvalhais, N., Chevallier, F., Gans, F., Goll, D.S., Haverd, V., Köhler, P., Ichii, K., Jain, A.K., Liu, J., Lombardozzi, D., Nabel, J.E.M.S., Nelson, J.A., O'Sullivan, M., Pallandt, M., Papale, D., Peters, W., Pongratz, J., Rödenbeck, C., Sitch, S., Tramontana, G., Walker, A., Weber, U., Reichstein, M., 2020. Scaling carbon fluxes from eddy covariance sites to globe: synthesis and evaluation of the FLUXCOM approach. Biogeosciences 17, 1343–1365.
Kalnay, E., Kanamitsu, M., Kistler, R., Collins, W., Deaven, D., Gandin, L., Iredell, M., Saha, S., White, G., Woollen, J., 1996. The NCEP/NCAR 40-year reanalysis project. Bulletin of the American meteorological Society 77, 437–472.
Kattge, J., Knorr, W., 2007. Temperature acclimation in a biochemical model of photosynthesis: a reanalysis of data from 36 species. Plant Cell Environ. 30, 1176–1190.
Keenan, T.F., Baker, I., Barr, A., Ciais, P., Davis, K., Dietze, M., Dragoni, D., Gough, C.M., Grant, R., Hollinger, D., Hufkens, K., Poulter, B., McCaughey, H., Raczka, B., Ryu, Y., Schaefer, K., Tian, H., Verbeeck, H., Zhao, M., Richardson, A.D., 2012. Terrestrial biosphere model performance for inter-annual variability of land-atmosphere CO2 exchange. Glob. Chang. Biol. 18, 1971–1987.
Keenan, T.F., Hollinger, D.Y., Bohrer, G., Dragoni, D., Munger, J.W., Schmid, H.P., Richardson, A.D., 2013. Increase in forest water-use efficiency as atmospheric carbon dioxide concentrations rise. Nature 499, 324–327.
Keenan, T.F., Prentice, I.C., Canadell, J.G., Williams, C.A., Wang, H., Raupach, M., Collatz, G.J., 2016. Recent pause in the growth rate of atmospheric CO2 due to enhanced terrestrial carbon uptake. Nat. Commun. 7, 13428.
Knauer, J., Zaehle, S., Reichstein, M., Medlyn, B.E., Forkel, M., Hagemann, S., Werner, C., 2017. The response of ecosystem water-use efficiency to rising atmospheric CO2 concentrations: sensitivity and large-scale biogeochemical implications. New Phytol. 213, 1654–1666.
Knohl, A., Baldocchi, D.D., 2008. Effects of diffuse radiation on canopy gas exchange processes in a forest ecosystem. J. Geophys. Res. Biogeosci. 113.
Kong, J., Ryu, Y., Liu, J., Dechant, B., Rey-Sanchez, C., Shortt, R., Szutu, D., Verfaillie, J., Houborg, R., Baldocchi, D.D., 2022. Matching high resolution satellite data and flux tower footprints improves their agreement in photosynthesis estimates. Agric. For. Meteorol. 316, 108878.
Kowalczyk, E., Wang, Y., Law, R., Davies, H., McGregor, J., Abramowitz, G., 2006. The CSIRO Atmosphere Biosphere Land Exchange (CABLE) model for use in climate models and as an offline model. CSIRO Marine and Atmospheric Research Paper 13, 42.
Kruse, O., Rupprecht, J., Mussgnug, J.H., Dismukes, G.C., Hankamer, B., 2005. Photosynthesis: a blueprint for solar energy capture and biohydrogen production technologies. Photochem.Photobiol.Sci. 4, 957–970.
Kyaw, T.P.U., 1987. Mathematical analysis of the operative temperature and energy budget. J. Therm. Biol. 12, 227–233.
Law, B.E., Falge, E., Gu, L., Baldocchi, D.D., Bakwin, P., Berbigier, P., Davis, K., Dolman, A.J., Falk, M., Fuentes, J.D., Goldstein, A., Granier, A., Grelle, A., Hollinger, D., Janssens, I.A., Jarvis, P., Jensen, N.O., Katul, G., Mahli, Y., Matteucci, G., Meyers, T., Monson, R., Munger, W., Oechel, W., Olson, R., Pilegaard, K., Paw, U.K.T., Thorgeirsson, H., Valentini, R., Verma, S., Vesala, T., Wilson, K., Wofsy, S., 2002. Environmental controls over carbon dioxide and water vapor exchange of terrestrial vegetation. Agric. For. Meteorol. 113, 97–120.
Leuning, R., Kelliher, F.M., Depury, D.G.G., Schulze, E.D., 1995a. Leaf nitrogen, photosynthesis, conductance and transpiration - scaling from leaves to canopies. Plant Cell Environ. 18, 1183–1200.
Leuning, R., Kelliher, F.M., Pury, D.G.G., Schulze, E.D., 1995b. Leaf nitrogen, photosynthesis, conductance and transpiration: scaling from leaves to canopies. Plant Cell Environ. 18, 1183–1200.
Li, F., Kustas, W.P., Anderson, M.C., Prueger, J.H., Scott, R.L., 2008. Effect of remote sensing spatial resolution on interpreting tower-based flux observations. Remote Sens. Environ. 112, 337–349.
Liu, Y., Liu, R., Chen, J.M., 2012. ChenRetrospective retrieval of long-term consistent global leaf area index (1981–2011) from combined AVHRR and MODIS data. J. Geophys. Res. Biogeosci. 117.
Lloyd, J., Taylor, J.A., 1994. On the temperature dependence of soil respiration. Funct. Ecol. 8, 315–323.
Luyssaert, S., Inglima, I., Jung, M., Richardson, A.D., Reichstein, M., Papale, D., Piao, S. L., Schulze, E.D., Wingate, L., Matteucci, G., Aragao, L., Aubinet, M., Beer, C., Bernhofer, C., Black, K.G., Bonal, D., Bonnefond, J.M., Chambers, J., Ciais, P., Cook, B., Davis, K.J., Dolman, A.J., Gielen, B., Goulden, M., Grace, J., Granier, A., Grelle, A., Griffis, T., GrÜNwald, T., Guidolotti, G., Hanson, P.J., Harding, R., Hollinger, D.Y., Hutyra, L.R., Kolari, P., Kruijt, B., Kutsch, W., Lagergren, F., Laurila, T., Law, B.E., Le Maire, G., Lindroth, A., Loustau, D., Malhi, Y., Mateus, J., Migliavacca, M., Misson, L., Montagnani, L., Moncrieff, J., Moors, E., Munger, J.W., Nikinmaa, E., Ollinger, S.V., Pita, G., Rebmann, C., Roupsard, O., Saigusa, N., Sanz, M.J., Seufert, G., Sierra, C., Smith, M.L., Tang, J., Valentini, R., Vesala, T., Janssens, I.A., 2007. CO2balance of boreal, temperate, and tropical forests derived from a global database. Glob. Chang. Biol. 13, 2509–2537.
Maes, W.H., Pagán, B.R., Martens, B., Gentine, P., Guanter, L., Steppe, K., Verhoest, N.E. C., Dorigo, W., Li, X., Xiao, J., Miralles, D.G., 2020. Sun-induced fluorescence closely linked to ecosystem transpiration as evidenced by satellite data and radiative transfer models. Remote Sens. Environ. 249, 112030.
Martens, B., Miralles, D.G., Lievens, H., van der Schalie, R., de Jeu, R.A.M., Fernández-Prieto, D., Beck, H.E., Dorigo, W.A., Verhoest, N.E.C., 2017. GLEAM v3: satellite-based land evaporation and root-zone soil moisture. Geosci. Model Dev. 10, 1903–1925.
Maxwell, R.M., Miller, N.L., 2005. Development of a coupled land surface and groundwater model. J. Hydrometeorol. 6, 233–247.
Migliavacca, M., Reichstein, M., Richardson, A.D., Colombo, R., Sutton, M.A., Lasslop, G., Tomelleri, E., Wohlfahrt, G., Carvalhais, N., Cescatti, A., Mahecha, M.D., Montagnani, L., Papale, D., Zaehle, S., Arain, A., Arneth, A., Black, T.A., Carrara, A., Dore, S., Gianelle, D., Helfter, C., Hollinger, D., Kutsch, W.L., Lafleur, P.M., Nouvellon, Y., Rebmann, C., Da Rocha, H.R., Rodeghiero, M., Roupsard, O., SebastiÀ, M.-T., Seufert, G., Soussana, J.-F., Van Der Molen, M.K., 2011.

Semiempirical modeling of abiotic and biotic factors controlling ecosystem respiration across eddy covariance sites. Glob. Chang. Biol. 17, 390–409.
Migliavacca, M., Reichstein, M., Richardson, A.D., Mahecha, M.D., Cremonese, E., Delpierre, N., Galvagno, M., Law, B.E., Wohlfahrt, G., Andrew Black, T., Carvalhais, N., Ceccherini, G., Chen, J., Gobron, N., Koffi, E., William Munger, J., Perez-Priego, O., Robustelli, M., Tomelleri, E., Cescatti, A., 2015. Influence of physiological phenology on the seasonal pattern of ecosystem respiration in deciduous forests. Glob. Chang. Biol. 21, 363–376.
Miralles, D.G., Holmes, T.R.H., De Jeu, R.A.M., Gash, J.H., Meesters, A.G.C.A., Dolman, A.J., 2011. Global land-surface evaporation estimated from satellite-based observations. Hydrol. Earth Syst. Sci. 15, 453–469.
Monfreda, C., Ramankutty, N., Foley, J.A., 2008. Farming the planet: 2. Geographic distribution of crop areas, yields, physiological types, and net primary production in the year 2000. Glob. Biogeochem. Cycles 22.
Moyano, F.E., Manzoni, S., Chenu, C., 2013. Responses of soil heterotrophic respiration to moisture availability: an exploration of processes and models. Soil Biol. Biochem. 59, 72–85.
Mu, Q., Zhao, M., Running, S.W., 2011. Improvements to a MODIS global terrestrial evapotranspiration algorithm. Remote Sens. Environ. 115, 1781–1800.
Myneni, R., Knyazikhin, Y., Park, T., 2015. MOD15A2H MODIS/Terra leaf area Index/FPAR 8-Day L4 global 500m SIN grid V006. NASA EOSDIS Land Processes DAAC.
Myneni, R., Knyazikhin, Y., Park, T., University, B., SIPS-NASA, M., 2015. MOD15A3H MODIS/Combined Terra+ Aqua Leaf Area Index/FPAR Daily L4 Global 500m SIN Grid. NASA EOSDIS Land Processes DAAC.
Pastorello, G., Trotta, C., Canfora, E., Chu, H., Christianson, D., Cheah, Y.-W., Poindexter, C., Chen, J., Elbashandy, A., Humphrey, M., Isaac, P., Polidori, D., Ribeca, A., van Ingen, C., Zhang, L., Amiro, B., Ammann, C., Arain, M.A., Ardö, J., Arkebauer, T., Arndt, S.K., Arriga, N., Aubinet, M., Aurela, M., Baldocchi, D., Barr, A., Beamesderfer, E., Marchesini, L.B., Bergeron, O., Beringer, J., Bernhofer, C., Berveiller, D., Billesbach, D., Black, T.A., Blanken, P.D., Bohrer, G., Boike, J., Bolstad, P.V., Bonal, D., Bonnefond, J.-M., Bowling, D.R., Bracho, R., Brodeur, J., Brümmer, C., Buchmann, N., Burban, B., Burns, S.P., Buysse, P., Cale, P., Cavagna, M., Cellier, P., Chen, S., Chini, I., Christensen, T.R., Cleverly, J., Collalti, A., Consalvo, C., Cook, B.D., Cook, D., Coursolle, C., Cremonese, E., Curtis, P.S., D'Andrea, E., da Rocha, H., Dai, X., Davis, K.J., De Cinti, B., de Grandcourt, A., De Ligne, A., De Oliveira, R.C., Delpierre, N., Desai, A.R., Di Bella, C. M., di Tommasi, P., Dolman, H., Domingo, F., Dong, G., Dore, S., Duce, P., Dufrêne, E., Dunn, A., Dušek, J., Eamus, D., Eichelmann, U., ElKhidir, H.A.M., Eugster, W., Ewenz, C.M., Ewers, B., Famulari, D., Fares, S., Feigenwinter, I., Feitz, A., Fensholt, R., Filippa, G., Fischer, M., Frank, J., Galvagno, M., Gharun, M., Gianelle, D., Gielen, B., Gioli, B., Gitelson, A., Goded, I., Goeckede, M., Goldstein, A. H., Gough, C.M., Goulden, M.L., Graf, A., Griebel, A., Gruening, C., Grünwald, T., Hammerle, A., Han, S., Han, X., Hansen, B.U., Hanson, C., Hatakka, J., He, Y., Hehn, M., Heinesch, B., Hinko-Najera, N., Hörtnagl, L., Hutley, L., Ibrom, A., Ikawa, H., Jackowicz-Korczynski, M., Janouš, D., Jans, W., Jassal, R., Jiang, S., Kato, T., Khomik, M., Klatt, J., Knohl, A., Knox, S., Kobayashi, H., Koerber, G., Kolle, O., Kosugi, Y., Kotani, A., Kowalski, A., Kruijt, B., Kurbatova, J., Kutsch, W.L., Kwon, H., Launiainen, S., Laurila, T., Law, B., Leuning, R., Li, Y., Liddell, M., Limousin, J.-M., Lion, M., Liska, A.J., Lohila, A., López-Ballesteros, A., López-Blanco, E., Loubet, B., Loustau, D., Lucas-Moffat, A., Lüers, J., Ma, S., Macfarlane, C., Magliulo, V., Maier, R., Mammarella, I., Manca, G., Marcolla, B., Margolis, H.A., Marras, S., Massman, W., Mastepanov, M., Matamala, R., Matthes, J.H., Mazzenga, F., McCaughey, H., McHugh, I., McMillan, A.M.S., Merbold, L., Meyer, W., Meyers, T., Miller, S.D., Minerbi, S., Moderow, U., Monson, R.K., Montagnani, L., Moore, C.E., Moors, E., Moreaux, V., Moureaux, C., Munger, J.W., Nakai, T., Neirynck, J., Nesic, Z., Nicolini, G., Noormets, A., Northwood, M., Nosetto, M., Nouvellon, Y., Novick, K., Oechel, W., Olesen, J.E., Ourcival, J.-M., Papuga, S.A., Parmentier, F.-J., Paul-Limoges, E., Pavelka, M., Peichl, M., Pendall, E., Phillips, R.P., Pilegaard, K., Pirk, N., Posse, G., Powell, T., Prasse, H., Prober, S.M., Rambal, S., Rannik, Ü., Raz-Yaseef, N., Reed, D., de Dios, V.R., Restrepo-Coupe, N., Reverter, B.R., Roland, M., Sabbatini, S., Sachs, T., Saleska, S.R., Sánchez-Cañete, E. P., Sanchez-Mejia, Z.M., Schmid, H.P., Schmidt, M., Schneider, K., Schrader, F., Schroder, I., Scott, R.L., Sedlák, P., Serrano-Ortíz, P., Shao, C., Shi, P., Shironya, I., Siebicke, L., Šigut, L., Silberstein, R., Sirca, C., Spano, D., Steinbrecher, R., Stevens, R.M., Sturtevant, C., Suyker, A., Tagesson, T., Takanashi, S., Tang, Y., Tapper, N., Thom, J., Tiedemann, F., Tomassucci, M., Tuovinen, J.-P., Urbanski, S., Valentini, R., van der Molen, M., van Gorsel, E., van Huissteden, K., Varlagin, A., Verfaillie, J., Vesala, T., Vincke, C., Vitale, D., Vygodskaya, N., Walker, J.P., Walter-Shea, E., Wang, H., Weber, R., Westermann, S., Wille, C., Wofsy, S., Wohlfahrt, G., Wolf, S., Woodgate, W., Li, Y., Zampedri, R., Zhang, J., Zhou, G., Zona, D., Agarwal, D., Biraud, S., Torn, M., Papale, D., 2020. The FLUXNET2015 dataset and the ONEFlux processing pipeline for eddy covariance data. Sci.Data 7, 225.
Paw, U.K.T., Gao, W., 1988. Applications of solutions to non-linear energy budget equations. Agric. For. Meteorol. 43, 121–145.
Peel, M.C., Finlayson, B.L., McMahon, T.A., 2007. Updated world map of the Köppen-Geiger climate classification. Hydrol. Earth Syst. Sci. 11, 1633–1644.
Piao, S., Wang, X., Wang, K., Li, X., Bastos, A., Canadell, J.G., Ciais, P., Friedlingstein, P., Sitch, S., 2020. Interannual variation of terrestrial carbon cycle: issues and perspectives. Glob. Chang. Biol. 26, 300–318.
Pike, J.G., 1964. The estimation of annual run-off from meteorological data in a tropical climate. J. Hydrol. 2, 116–123.
Priestley, C.H.B., Taylor, R.J., 1972. On the assessment of surface heat flux and evaporation using large-scale parameters. MWRv 100, 81–92.
Restrepo-Coupe, N., Levine, N.M., Christoffersen, B.O., Albert, L.P., Wu, J., Costa, M.H., Galbraith, D., Imbuzeiro, H., Martins, G., da Araujo, A.C., 2017. Do dynamic global vegetation models capture the seasonality of carbon fluxes in the Amazon basin? A data-model intercomparison. Glob. Chang. Biol. 23, 191–208.
Rodell, M., Houser, P., Jambor, U., Gottschalck, J., Mitchell, K., Meng, C.-J., Arsenault, K., Cosgrove, B., Radakovich, J., Bosilovich, M., 2004. The global land data assimilation system. Bull. Am. Meteorol. Soc. 85, 381–394.
Running, S.W., Nemani, R.R., Heinsch, F.A., Zhao, M., Reeves, M., Hashimoto, H., 2004. A continuous satellite-derived measure of global terrestrial primary production. BioSc 54, 547–560.
Ryu, Y., Baldocchi, D.D., Black, T.A., Detto, M., Law, B.E., Leuning, R., Miyata, A., Reichstein, M., Vargas, R., Ammann, C., Beringer, J., Flanagan, L.B., Gu, L., Hutley, L.B., Kim, J., McCaughey, H., Moors, E.J., Rambal, S., Vesala, T., 2012. On the temporal upscaling of evapotranspiration from instantaneous remote sensing measurements to 8-day mean daily-sums. Agric. For. Meteorol. 152, 212–222.
Ryu, Y., Baldocchi, D.D., Kobayashi, H., van Ingen, C., Li, J., Black, T.A., Beringer, J., van Gorsel, E., Knohl, A., Law, B.E., Roupsard, O., 2011. Integration of MODIS land and atmosphere products with a coupled-process model to estimate gross primary productivity and evapotranspiration from 1 km to global scales. Global Biogeochem Cycles 25.
Ryu, Y., Berry, J.A., Baldocchi, D.D., 2019. What is global photosynthesis? History, uncertainties and opportunities. Remote Sens. Environ. 223, 95–114.
Ryu, Y., Jiang, C., Kobayashi, H., Detto, M., 2018. MODIS-derived global land products of shortwave radiation and diffuse and total photosynthetically active radiation at 5km resolution from 2000. Remote Sens. Environ. 204, 812–825.
Schaffer, C., 1993. Selecting a classification method by cross-validation. MLear 13, 135–143.
Schwalm, C.R., Black, T.A., Amiro, B.D., Arain, M.A., Barr, A.G., Bourque, C.P.A., Dunn, A.L., Flanagan, L.B., Giasson, M.-A., Lafleur, P.M., Margolis, H.A., McCaughey, J.H., Orchansky, A.L., Wofsy, S.C., 2006. Photosynthetic light use efficiency of three biomes across an east–west continental-scale transect in Canada. Agric. For. Meteorol. 140, 269–286.
Shan, N., Zhang, Y., Chen, J.M., Ju, W., Migliavacca, M., Peñuelas, J., Yang, X., Zhang, Z., Nelson, J.A., Goulas, Y., 2021. A model for estimating transpiration from remotely sensed solar-induced chlorophyll fluorescence. Remote Sens. Environ. 252, 112134.
Simard, M., Pinto, N., Fisher, J.B., Baccini, A., 2011. Mapping forest canopy height globally with spaceborne lidar. J. Geophys. Res. Biogeosci. 116.
Sitch, S., Friedlingstein, P., Gruber, N., Jones, S.D., Murray-Tortarolo, G., Ahlström, A., Doney, S.C., Graven, H., Heinze, C., Huntingford, C., Levis, S., Levy, P.E., Lomas, M., Poulter, B., Viovy, N., Zaehle, S., Zeng, N., Arneth, A., Bonan, G., Bopp, L., Canadell, J.G., Chevallier, F., Ciais, P., Ellis, R., Gloor, M., Peylin, P., Piao, S.L., Le Quéré, C., Smith, B., Zhu, Z., Myneni, R., 2015. Recent trends and drivers of regional sources and sinks of carbon dioxide. Biogeosciences 12, 653–679.
Smith, N.G., Keenan, T.F., Colin Prentice, I., Wang, H., Wright, I.J., Niinemets, Ü., Crous, K.Y., Domingues, T.F., Guerrieri, R., Yoko Ishida, F., Kattge, J., Kruger, E.L., Maire, V., Rogers, A., Serbin, S.P., Tarvainen, L., Togashi, H.F., Townsend, P.A., Wang, M., Weerasinghe, L.K., Zhou, S.-X., 2019. Global photosynthetic capacity is optimized to the environment. Ecol. Lett. 22, 506–517.
Sposito, G., 2017. Understanding the budyko equation. Water 9, 236.
Still, C.J., Berry, J.A., Collatz, G.J., DeFries, R.S., 2003. Global distribution of C3 and C4 vegetation: carbon cycle implications. Glob. Biogeochem. Cycles 17, 6-1-6-14.
Stocker, B.D., Wang, H., Smith, N.G., Harrison, S.P., Keenan, T.F., Sandoval, D., Davis, T., Prentice, I.C., 2020. P-model v1.0: an optimality-based light use efficiency model for simulating ecosystem gross primary production. Geosci. Model Dev. 13, 1545–1581.
Stocker, B.D., Zscheischler, J., Keenan, T.F., Prentice, I.C., Peñuelas, J., Seneviratne, S.I., 2018. Quantifying soil moisture impacts on light use efficiency across biomes. New Phytol. 218, 1430–1449.
Tang, S., Wang, X., He, M., Huang, L., Zhang, Y., Yang, H., Piao, S., 2020. Global patterns and climate controls of terrestrial ecosystem light use efficiency. J. Geophys. Res. Biogeosci. 125 e2020JG005908.
Tagesson, T., Tian, F., Schurgers, G., Horion, S., Scholes, R., Ahlstrom, A., Ardo, J., Moreno, A., Madani, N., Olin, S., Fensholt, R., 2021. A physiology-based Earth observation model indicates stagnation in the global gross primary production during recent decades. Glob. Chang. Biol. 27, 836–854.
Tang, X., Li, H., Desai, A.R., Nagy, Z., Luo, J., Kolb, T.E., Olioso, A., Xu, X., Yao, L., Kutsch, W., Pilegaard, K., Köstner, B., Ammann, C., 2014. How is water-use efficiency of terrestrial ecosystems distributed and changing on Earth? Sci. Rep. 4, 7483.
Tao, X., Cui, J., Dai, Y., Wang, Z., Xu, X., 2016. Soil respiration responses to soil physiochemical properties in urban different green-lands: a case study in Hefei, China. Int.Soil Water Conserv.Res. 4, 224–229.
Tramontana, G., Jung, M., Schwalm, C.R., Ichii, K., Camps-Valls, G., Ráduly, B., Reichstein, M., Arain, M.A., Cescatti, A., Kiely, G., Merbold, L., Serrano-Ortiz, P., Sickert, S., Wolf, S., Papale, D., 2016. Predicting carbon dioxide and energy fluxes across global FLUXNET sites with regression algorithms. Biogeosciences 13, 4291–4313.
Walker, A.P., Quaife, T., van Bodegom, P.M., De Kauwe, M.G., Keenan, T.F., Joiner, J., Lomas, M.R., MacBean, N., Xu, C., Yang, X., Woodward, F.I., 2017. The impact of alternative trait-scaling hypotheses for the maximum photosynthetic carboxylation rate (Vcmax) on global gross primary production. New Phytol. 215, 1370–1386.
Wang, H., Prentice, I.C., Keenan, T.F., Davis, T.W., Wright, I.J., Cornwell, W.K., Evans, B. J., Peng, C., 2017a. Towards a universal model for carbon dioxide uptake by plants. Nat.Plants 3, 734–741.
Wang, L., Zhu, H., Lin, A., Zou, L., Qin, W., Du, Q., 2017b. Evaluation of the latest MODIS GPP products across multiple biomes using global Eddy covariance flux data. Remote Sens. 9, 418.

Waring, R., Landsberg, J., Williams, M., 1998. Net primary production of forests: a constant fraction of gross primary production? Tree Physiol. 18, 129–134.
Wei, S., Fang, H., Schaaf, C.B., He, L., Chen, J.M., 2019. Global 500 m clumping index product derived from MODIS BRDF data (2001–2017). Remote Sens. Environ. 232, 111296.
Weiss, A., Norman, J.M., 1985. Partitioning solar radiation into direct and diffuse, visible and near-infrared components. Agric. For. Meteorol. 34, 205–213.
Wild, M., Folini, D., Hakuba, M.Z., Schär, C., Seneviratne, S.I., Kato, S., Rutan, D., Ammann, C., Wood, E.F., König-Langlo, G., 2015. The energy balance over land and oceans: an assessment based on direct observations and CMIP5 climate models. Clim. Dyn. 44, 3393–3429.
Williams, C.A., Reichstein, M., Buchmann, N., Baldocchi, D., Beer, C., Schwalm, C., Wohlfahrt, G., Hasler, N., Bernhofer, C., Foken, T., Papale, D., Schymanski, S., Schaefer, K., 2012. Climate and vegetation controls on the surface water balance: synthesis of evapotranspiration measured across a global network of flux towers. Water Resour. Res. 48.
Wong, S.C., Cowan, I.R., Farquhar, G.D., 1979. Stomatal conductance correlates with photosynthetic capacity. Nature 282, 424–426.
Xue, B.-L., Guo, Q., Otto, A., Xiao, J., Tao, S., Li, L., 2015. Global patterns, trends, and drivers of water use efficiency from 2000 to 2013. Ecosphere 6, art174.
Yang, S., Zhang, J., Zhang, S., Wang, J., Bai, Y., Yao, F., Guo, H., 2020. The potential of remote sensing-based models on global water-use efficiency estimation: an evaluation and intercomparison of an ecosystem model (BESS) and algorithm (MODIS) using site level and upscaled eddy covariance data. Agric. For. Meteorol. 287, 107959.
Yao, Y., Liang, S., Li, X., Hong, Y., Fisher, J.B., Zhang, N., Chen, J., Cheng, J., Zhao, S., Zhang, X., Jiang, B., Sun, L., Jia, K., Wang, K., Chen, Y., Mu, Q., Feng, F., 2014. Bayesian multimodel estimation of global terrestrial latent heat flux from eddy covariance, meteorological, and satellite observations. J.Geophys.Res.Atmos. 119, 4521–4545.
Yuan, W., Liu, S., Yu, G., Bonnefond, J.-M., Chen, J., Davis, K., Desai, A.R., Goldstein, A. H., Gianelle, D., Rossi, F., Suyker, A.E., Verma, S.B., 2010. Global estimates of evapotranspiration and gross primary production based on MODIS and global meteorology data. Remote Sens. Environ. 114, 1416–1431.
Yuan, W., Luo, Y., Li, X., Liu, S., Yu, G., Zhou, T., Bahn, M., Black, A., Desai, A.R., Cescatti, A., Marcolla, B., Jacobs, C., Chen, J., Aurela, M., Bernhofer, C., Gielen, B., Bohrer, G., Cook, D.R., Dragoni, D., Dunn, A.L., Gianelle, D., Grünwald, T., Ibrom, A., Leclerc, M.Y., Lindroth, A., Liu, H., Marchesini, L.B., Montagnani, L., Pita, G., Rodeghiero, M., Rodrigues, A., Starr, G., Stoy, P.C., 2011. Redefinition and global estimation of basal ecosystem respiration rate. Global Biogeochem Cycles 25.
Zeng, J., Matsunaga, T., Tan, Z.-H., Saigusa, N., Shirai, T., Tang, Y., Peng, S., Fukuda, Y., 2020. Global terrestrial carbon fluxes of 1999–2019 estimated by upscaling eddy covariance data with a random forest. Sci.Data 7, 313.
Zhang, K., Kimball, J.S., Nemani, R.R., Running, S.W., 2010. A continuous satellite-derived global record of land surface evapotranspiration from 1983 to 2006. Water Resour. Res. 46.
Zhang, K., Kimball, J.S., Nemani, R.R., Running, S.W., Hong, Y., Gourley, J.J., Yu, Z., 2015. Vegetation greening and climate change promote multidecadal rises of global land evapotranspiration. Sci. Rep. 5, 15956.
Zhang, Y., Song, C., Sun, G., Band, L.E., McNulty, S., Noormets, A., Zhang, Q., Zhang, Z., 2016. Development of a coupled carbon and water model for estimating global gross primary productivity and evapotranspiration based on eddy flux and remote sensing data. Agric. For. Meteorol. 223, 116–131.
Zhang, Y., Xiao, X., Wu, X., Zhou, S., Zhang, G., Qin, Y., Dong, J., 2017. A global moderate resolution dataset of gross primary production of vegetation for 2000–2016. Sci.Data 4, 170165.
Zhang, Y., Yu, Q., Jiang, J.I.E., Tang, Y., 2008. Calibration of Terra/MODIS gross primary production over an irrigated cropland on the North China plain and an alpine meadow on the Tibetan plateau. Glob. Chang. Biol. 14, 757–767.
Zscheischler, J., Mahecha, M.D., Avitabile, V., Calle, L., Carvalhais, N., Ciais, P., Gans, F., Gruber, N., Hartmann, J., Herold, M., Ichii, K., Jung, M., Landschützer, P., Laruelle, G.G., Lauerwald, R., Papale, D., Peylin, P., Poulter, B., Ray, D., Regnier, P., Rödenbeck, C., Roman-Cuesta, R.M., Schwalm, C., Tramontana, G., Tyukavina, A., Valentini, R., van der Werf, G., West, T.O., Wolf, J.E., Reichstein, M., 2017. Reviews and syntheses: an empirical spatiotemporal description of the global surface–atmosphere carbon fluxes: opportunities and data limitations. Biogeosciences 14, 3685–3703.